

Safe use of Robotic Arms as Input Devices

A.I. (Adrian Ion) Lazar

MSc Report

Committee:

Prof.dr.ir. G.J.M. Krijnen

Dr.ir. D. Dresscher

Dr.ir. A.Q.L. Keemink

May 2019

015RAM2019
Robotics and Mechatronics
EE-Math-CS
University of Twente
P.O. Box 217
7500 AE Enschede
The Netherlands

Abstract

The independent research centre i-Botics, founded by TNO and University of Twente, currently uses the omega.7 haptic device as a master for the telemanipulation of the KUKA LWR 4+ robotic arm as a slave device for tasks that need to be performed in a dangerous or hostile environment for human operators.

To improve this state of the art, the Emika Franka Panda robotic arm is, herein, proposed as replacement for the omega.7 device. Since human operators are to physically interact with the Panda robotic arm, strict safety measures prompt for proper energy, force and power limitations to be carefully set. The novel master device needs to also fulfil the requirements of a haptic input device.

Herein, a control methodology was developed and implemented such that the necessary safety and haptic prerequisites are met. The system successfully passed the four evaluation tests that addressed its haptic performance and safety. Although the slave device was used as a Gazebo simulation of the KUKA LWR 4+ robotic arm, the design is also valid and recommended for the real hardware.

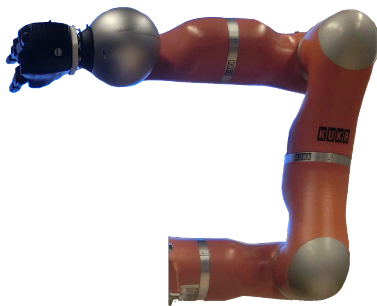
Contents

1 Introduction	1
1.1 Context	1
1.2 Problem statement	1
1.3 Project goals	1
1.4 Report outline	2
2 Analysis	3
2.1 Safety aspects	3
2.2 Haptic interface aspects	10
3 Design and implementation	18
3.1 Current bilateral telemanipulation system	18
3.2 Panda haptic device within the bilateral telemanipulation system	19
3.3 Implementation in ROS	21
4 Evaluation	24
4.1 General setup and methods	24
4.2 Test 1 - A transparency test - The haptic performance	25
4.3 Test 2 - A safety test - The energy limit	30
4.4 Test 3 - A safety test -The power limit	33
4.5 Test 4 - A safety test - The force limit	35
4.6 Evaluation conclusion	36
5 Conclusion and recommendations	38
5.1 Conclusions	38
5.2 Recommendations	39
A Screw theory applied to human arm kinematics	40
A.1 Building the geometrical Jacobian	40
A.2 Pseudo-code for obtaining the maximum force	41
B Results for test 2 - A safety test - The energy limit	43
Bibliography	44

1 Introduction

1.1 Context

i-Botics is an open innovation centre for Research and Development in Interaction Robotics. The independent research centre has been founded by TNO and University of Twente and aims at developing knowledge and technology for value adding Robotic solutions. One of the topics on which research and development is taken further within i-Botics, is telepresence (remote “being”) and telemanipulation (remote “operation”, “handling”). A typical scenario consists of a complex task that needs to be performed in a dangerous or hostile environment for a human operator to work in. Yet, for the complex task human abilities as judging a situation based on perception and dexterity are essential. The interface that the operator uses to control the robotic system and receive (haptic) feedback is an important part of a telemanipulation system. Currently, a Force Dimension omega.7 haptic device is used to control a KUKA LWR 4+ robotic arm with an attached RightHand Robotics ReFlex TakkTile robotic hand (see Figure 1.1).



(a) The KUKA LWR 4+ robotic arm with an attached RightHand Robotics ReFlex TakkTile robotic hand.¹



(b) The Omega.7 haptic device. From ForceDimension (2019).

Figure 1.1: Current i-Botics bilateral telemanipulation setup.

1.2 Problem statement

The omega.7 is possibly the world’s most advanced desktop 7-DOF haptic interface to date, making it a good option for controlling a KUKA LWR 4+ robotic arm. Nonetheless, there are still a few drawbacks: (1) a workspace smaller than that of the KUKA LWR 4+; (2) its inability to receive feedback from the KUKA LWR 4+ on the 3 of the 6 degrees of freedom, namely, the rotational ones; (3) only one degree of freedom for end-effector grasping control.

1.3 Project goals

The goal of this project is to provide an alternative to the Omega.7 haptic device for the telemanipulation of the KUKA LWR 4+ robotic arm to be used safely by humans that need to use telepresence to avoid working in dangerous or hostile locations. The main research questions of this project are:

1. *"How can the Panda robotic arm be safely used in interaction with humans?"*
2. *"How can the Panda robotic arm be effectively used as a haptic interface device?"*

Herein, I bring forward an improvement to the current limitations of the system, by replacing the omega.7 haptic device with another a robotic arm (i.e. the Emika Franka Panda robotic

¹Source: <https://www.ram.ewi.utwente.nl/research/project/i-botics.html>

arm). This novel use of a robotic arm as an input haptic device to control the KUKA LWR 4+s, since the robotic arms are usually used as output devices (e.g. pick and place tasks, welding (Erden and Billard, 2014) etc).

The advantages of the Panda robotic arm as input haptic device over the omega.7 are: (1) a larger workspace; (2) its ability to receive feedback from the KUKA LWR 4+ on all 6 degrees of freedom, including, the 3 rotational ones; (3) may have more than one degree of freedom for end-effector grasping control, by attaching an exoskeleton hand, for example.

1.4 Report outline

This thesis report is organized in 5 chapters. The first is a brief introduction to the research topic assignment containing the context, problems to be tackled with and the project goal. The second chapter is an analysis performed on the safety and haptic aspects of the proposed alternative for the current state of the art. The design and implementation of the solutions that resulted from the analysis chapter are then presented in Chapter 3. In Chapter 4, four tests are detailed as part of the evaluation. Their design and results are presented. Finally, Chapter 5 presents the conclusions of this research, followed by recommendations for future work.

2 Analysis

In this chapter the use of the Panda robotic arm is analysed in terms safety and haptic aspects. For safety, the physical interaction and mechanical interface standards are considered. For the use of the robotic arm as an input haptic device, the optimal workspace and the continuous force are discussed in terms of the performance criteria reported by Sun et al. (2017).

2.1 Safety aspects

2.1.1 Safe physical interaction

The interaction between a human and a robotic arm is part of a broader topic known in literature as "Human-Robot Interaction" (HRI). This wide topic includes the collaboration, communication, and cooperation between humans and robots. The interaction types can be classified as: (1) physical Human-Robot Interaction (pHRI) and (2) social and cognitive aspects of Human-Robot Interactions (cHRI). For the first class of human-robot interactions, safety involves preventing harmful collisions between humans and robots operating within a shared space. For the safety of the second class of interactions, the focus is on preventing the indirect, psychological harms such as stress, psychological discomfort and robotic violation of social conventions and norms during interaction (Mumm and Mutlu, 2011; Butler and Agah, 2001). Methods for such pHRI safety are summarized in Lasota et al. (2017), along with methods for the cHRI safety. However, in this research the focus is on the pHRI and Haddadin and Croft (2016) gives an overview on the state of the art in pHRI.

Safety Standards for HRI

Safety for industrial robots is addressed in a variable of general standards, developed and published by the International Organization for Standardization (ISO) (Haddadin and Croft, 2016):

- ISO 12100:2010 Safety of Machinery - General Principles for Design - Risk Assessment and Risk Reductions.
- ISO 13849-1:2008 Safety of Machinery - Safety-Related Parts of Control Systems - Part 1: General Principles for Design (ISO13849, 2008).
- ISO 13855:2010 Safety of Machinery - Positioning of Safeguards With Respect to the Approach Speeds of Parts of the Human Body.
- ISO 10218:2011 Robots and robotic devices - Safety requirements for industrial robots.
- ISO/TS 15066:2016 Robots and robotic devices - Collaborative robots.

The most important industrial robotics standard is the ISO 10218. It was established in the recognition of the particular hazards that are presented by industrial robots and industrial robot systems. It is divided in two parts. The first part titled "Part 1: Robots" (ISO10218-1, 2011) is particularly dedicated to manufacturers as it covers the robot only. While second part, titled "Part 2: Robot systems and integration" (ISO10218-2, 2011) provides safety requirements for the integration of industrial robots and industrial robot systems and industrial robot cell(s).

Recent updates to ISO 10218 led to development of new technical specification ISO/TS15066 (2016). It provides guidance for collaborative robot operation where a robot and a human share the same workspace. This document specifies that 140N is the maximum value allowed for the force corresponding to the human-robot interaction that takes place at hands level.

Properties of a robot designed for physical Human-Robot Interaction (pHRI)

In order to talk about safe interactions between robots and human, certain properties are desirable from a hardware perspective. The properties of a robot designed for physical Human-Robot Interaction (pHRI) are:

- Lightweight design - enables mobility by optimizing the weight reduction of the entire system (including controllers, power supply) (Haddadin and Croft, 2016) and reduces any possible injury that may arise in case of a collision with a human (Tadele, 2014).
- Flexible actuators design - allows reducing the stiffness between an actuator and its load. This results in the following advantages: greater shock tolerance, lower reflected inertia by decoupling the motor side from the link-side inertia, more stable and accurate force control in addition to the capacity for storing and releasing energy (Meguenani, 2017).
- Proprioceptive Force/Torque Sensing - allows for contact sensing along the entire robot structure with measurements of contact magnitude, direction, and knowledge of which link was contacted (Haddadin et al., 2008; Haddadin and Croft, 2016).
- Visual motion tracking - achieves real-time collision avoidance (Flacco et al., 2012) by tracking and planning the location of a human partner and predicting its future location. This feature is not desirable for the goal of this research, where the human is in contact with the robotic arm during operation time. However, it is an important property to consider when discussing pHRI in general.

Energy based safety metric constrain

During the physical interaction between a human and a robotic arm two parameters are source of danger, for a given shape of the contact surface: the impact peak force created at collision and the contact force generated after the establishment of a physical contact. The most generic way to include and consider these parameters for guaranteeing safe interaction is to use energy.

The energy is a universal quantity that can describe any physical incidents occurring during human-robot interaction. For example, the impact peak force is directly related to the amount of kinetic energy dissipated at collision and the contact forces mostly derive from the amount of potential energy that accumulates in controller of the robot during physical contact. Inertia, velocity and also the resulting position error during physical contact are all part of the mathematical expression that describes the dynamics of the controller robot and hence the energy. Safety during human-robot interaction can therefore be ensured by modulating the amount of energy instantaneously deployed by the robot (Meguenani, 2017). Tadele (2014) proposed and tested in a simulation environment a safety layer for a multiple degree of freedom manipulator that modulates the energy by injecting damping in the joint space, when an impedance controller is used. The total energy in the system is defined as the sum of the kinetic energy of the manipulator and the potential energy due to the spatial spring, as part of the impedance controller used. The reasons for using energy as a criteria safety follow the work of Wood (1971) and Yoganandan et al. (1996) that identified the maximum allowed energy that can causes head injuries. Thus, the energy limits defined for the specific types of injuries are:

$$E_{\text{limit}} = \begin{cases} 517\text{J} & \text{Adult cranium bone failure} & (2.1) \\ 127\text{J} & \text{Infant cranium bone failure} & (2.2) \\ 35\text{J} & \text{Neck fracture} & (2.3) \end{cases}$$

Moreover, Haddadin and Croft (2016) conducted collision experiments with a KUKA/DLR light-weight robot and a systematic injury and pain analysis. They investigated the relationships

between measured impact characteristics and quantities (i.e. impact peak force, impact area, tissue displacement, tissue stiffness, stress, impact velocity, kinetic energy, and energy density) and output parameters, such as pain and injury. The impact area is on the lateral surface of the right upper arm of a young adult. During the tests, the reflected mass was kept constant at 3.75 kg and the impactor was a sphere with a radius of 12.5 mm. The injury was defined using AO-classification (Ruedi et al., 2007) after each impact. All impacts were carried out at the same location on the human body at increasing impact velocity until the participant stopped the experiment as the pain limit was reached. The pain tolerance was recorded on the visual analogue scale (VAS). The maximum force recorded during the impact experiments that did not cause a bruise was at an impact peak force of 272.2 N, impact velocity of 2.55 m/s, resulting in a kinetic energy of 12.2 J and pain tolerance in a VAS of 6/10. However, for the context of this assignment, the border limit is not of interest, and more important are the results that correspond to little to no pain. These results score a maximum of 2/10 on the visual analogue scale (VAS) and are summarized in Table 2.1. For more information regarding the experimental tests refer to page 1843 of Haddadin and Croft (2016).

VAS (x/10)	Impact peak force (N)	Impact velocity (m/s)	Kinetic energy (J)
0	9.50	0.20	0.08
0	59.60	0.88	1.45
1	81.40	1.11	2.31
1.5	103.50	1.34	3.37
2	128.10	1.55	4.50

Table 2.1: The impact data for the lateral surface of the right upper arm. Taken from Table 69.5 Haddadin and Croft (2016).

Herein, the energy limit of 4.5 J will be used for implementation because it is a trade-off between safety and performance.

Power based safety metric constrain

Another safety metric that can be considered besides the total energy of the system can be one based on the peak power, such as the Head Impact Power (HIP) proposed by Newman and Shewchenko (2000). They investigated and presented the probabilities and the related power values of a concussion from the reconstruction of football helmeted head impacts using crash test dummies. The power limits are then defined as:

$$P_{\text{limit}} = \begin{cases} 12 \text{ kW} & \text{Frontal Impacts} \\ 10 \text{ kW} & \text{Non-Frontal Impacts} \end{cases} \quad (2.4)$$

Tadele (2014) uses this power based safety metric in his work where he simulates the performances for limiting the power to 0.5 W and 1 W. Based on his work, Raiola et al. (2018) implemented and validated it with experiments where the power limit is set to 2 W. Using the Table 2.1 and the equation 2.6, the impact maximum peak power can be calculated. The safety criteria limits are summarize in Table 2.2. These safety limits will have to allow good haptic performance that is analysed in following section 2.2.

$$P = F * v \quad (2.6)$$

VAS (x/10)	Impact peak power (W)	Kinetic energy (J)
0	1.90	0.08
0	52.44	1.45
1	90.35	2.31
1.5	138.69	3.37
2	198.55	4.50

Table 2.2: Energy and power limits that guarantee safe HRI with respect to a pain tolerance scale (VAS) as investigated by Haddadin and Croft (2016).

Geo-fencing constrain

The geo-fencing constrain can add value to the overall system safety. In the ISO/TS15066 (2016), this constrain is referred as separation monitor. There are certain areas in the shared workspace of the human and robot that the robot should not be allowed to enter. For example, if the human operator is sitting on a chair while controlling the robotic arm, then this chair area would be such an area that the robot should not be allowed to enter. In other words, any static predefined area within the reachable workspace of the robotic arm should be protected by adjustable virtual walls. These will help prevent the robot collisions that could damage the hardware and injure the user.

Similarly, Radi and Reinhart (2009) implemented virtual walls as a safety strategy and unlike our application, the walls are defined on the remote environment for their industrial haptic robot guidance system. As a consequence, stability is not guaranteed during the contact between the robot and the virtual walls. If the communication channel between the user and remote sides contains time delays, this channel will be an active element in the system and will lead to instability. However, considering the context of this assignment, the virtual wall is located on the user side and time delays are not expected.

2.1.2 Safe physical interaction using a Panda robotic arm

The safety aspects covered in Section 2.1.1 are investigated with respect to the robotic arm chosen for this assignment, i.e. Panda robotic arm.

Description of the Panda robotic arm

The Panda robotic arm is a 7-DOF robotic arm manufactured by Franka Emika GmbH, a spin-off resulted from SAPHARI Project (Safe and Autonomous Physical Human-Aware Robot Interaction) and German Space Agency (DLR). The C.E.O. of Franka Emika GmbH is Prof. Dr.-Ing. Sami Haddadin, who is also currently the director of the Chair of Robotics Science and System Intelligence at TUM ¹. He is also the co-author of the Chapter "Physical Human-Robot Interaction" (Haddadin and Croft, 2016) that gives an overview of the state of the art in pHRI. Figure 2.1 presents an overview of the location, orientation and name of the seven joints and Table 2.3 gives an overview of range, maximum speed and maximum torque of these joints.

The Panda robotic arm can be controlled through two modes: the desktop mode and the research mode. The desktop mode allows the user to interact through a website interface where pick-and-place tasks and joint or Cartesian space motions can be commanded. On the other side, the research mode offers access to the hardware for designing and implementing custom controllers. For this assignment, the research mode is used.

¹<https://www.ei.tum.de/en/structure-and-profile/directory/professors/haddadin/>

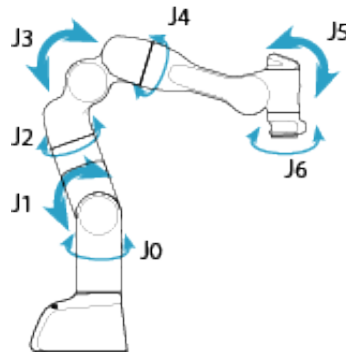


Figure 2.1: Overview of joint configuration in the Panda robotic arm (EMIKA, 2018).

Joint name	Maximum torque (Nm)	Range of motion (°)	Maximum velocity (°/s)
J0	87	±166	150
J1	87	±101	150
J2	87	±166	150
J3	87	-176/ -4	150
J4	12	±166	180
J5	12	-1/215	180
J6	12	±166	180

Table 2.3: Panda maximum ratings per joint (EMIKA, 2018).

Safety Standards for HRI

According to the available data-sheet EMIKA (2017) and EMIKA (2018), the robotic arm is "PL d cat. 3 (EN ISO 13849-1:2008)" (ISO13849, 2008) certified, with the following safety functions:

- safe stop - also known as protective stop is a type of interruption of operation that allows a stoppage of motion for safeguarding purposes and which retains the program logic to facilitate a restart (definition 3.17 in ANSI/RIA-R15.06 (2012));
- safety-rated monitored stop - condition where the robot is stopped with drive power active, while a monitoring system with a specified sufficient safety performance ensures that the robot does not move (definition 3.19.6 in ANSI/RIA-R15.06 (2012));
- safety-rated monitored speed - safety-rated function that causes a protective stop when either the Cartesian speed of a point relative to the robot flange (e.g. the gripper end-effector of Panda), or the speed of one or more axes exceeds a specified limit value (definition 3.19.1 in ANSI/RIA-R15.06 (2012));
- safety-rated soft axis and space limiting - where soft limits are software-defined limits to robot motion and space limiting is used to define any geometric shape which either limits robot motion within the defined space, or prevents the robot from entering the defined space (definition 3.19.3 in ANSI/RIA-R15.06 (2012));

With regards to the most important standards (i.e. ISO/TS15066 (2016) and ISO10218-2 (2011)), Panda does not officially mention any of them.

Properties of the Panda robotic arm designed for physical Human-Robot Interaction (pHRI)

The Panda robotic arm is advertised as collaborative robot system, designed to work among humans. It features three out of the four most important desirable properties a robotic arm can incorporate in its design in order to achieve safe pHRI:

- Lightweight design - with 18 kg of weight, the Panda robotic arm is considered to be lightweight (Haddadin and Croft, 2016).
- Flexible actuators design - based on modular sensor-actuator units (Rader et al., 2017).
- Proprioceptive Force/Torque Sensing - equipped with torque sensors in all 7 axes.

Contact and collision detection as safety metric constrain

The Panda robotic arm does not have any energy and/or power constraints. However, more on the low level hardware, the manufacturer provides other safety-like feature. Within the software library (i.e. `libfranka`²), there is a possibility to set torque boundaries for each joint of the robotic arm and a wrench boundary defined in Cartesian space. These boundaries are defined for contact and collision separately and the difference lies in the way the robotic arm reacts. Contact is triggered only when the user applies a force or torque whose magnitude lies between the lower and upper thresholds, and collision is triggered when that force or torque is higher the higher threshold. When a collision is registered, the robotic arm stops and a reset is required, by calling the function `franka_control::ErrorRecoveryAction`.

The `franka_ros` metapackage integrates the `libfranka` into Robot Operating System (ROS) middleware and ROS control software framework. Through this `franka_ros` interface, two ways of setting these torque and wrench boundaries can be chosen from:

- Set **common** torque and wrench boundaries for acceleration/deceleration and constant velocity movement phases. Therefore, 4 input parameters are required:
 - `"lower_torque_thresholds"` - the contact torque thresholds for each joint in N m.
 - `"upper_torque_thresholds"` - the collision torque thresholds for each joint in N m.
 - `"lower_force_thresholds"` - the contact wrench threshold defined as a six component vector, where the first three values are X, Y, Z forces in N and the next three values are torques around X, Y, Z axis in N m.
 - `"upper_force_thresholds"` - the collision wrench threshold defined as a six component vector, where the first three values are X, Y, Z forces in N and the next three values are torques around X, Y, Z axis in N m.
- Set **separate** torque and wrench boundaries for acceleration/deceleration and constant velocity movement phases. Therefore, 8 input parameters are required: the same 4 parameters from above, expressed in 2 cases:
 - the robotic arm is in acceleration/deceleration phase ($\text{acceleration} \neq 0$)
 - the robotic arm is in constant velocity movement phases ($\text{acceleration} = 0$)

To use this feature, the **common** torque and wrench boundaries are defined. For the torque boundaries of each joint, the lower and upper values were set to the maximum torque of each joint because explicit values for limiting the joint space of a multiple degree of freedom serial chain manipulator were not found in literature and limiting the wrench in Cartesian space would limit the torques in joint space as a consequence. Similarly, explicit limits for the torque component of the wrench boundary were not found in literature and, therefore, a large enough, meaningless limit was set. However, for the force component of the wrench boundary, ISO/TS15066 (2016) provides the maximum contact force of 140N defined as the maximum magnitude vector force. Therefore, a system is required to compute the magnitude and limit the force before exceeding the maximum allowed 140N (ISO/TS15066, 2016). Although such a system will be implemented, for the final system, a conservative measure is taken by using the

²<https://frankaemika.github.io/libfranka/index.html>

Panda's library to limit the maximum force on each of the three axis to $80\text{N} (\sqrt{140^2/3})$, such that the combined force vector is always lower than 140N .

Geo-fencing constrain

The geo-fencing feature as discuss in section 2.1.1 consist of preventing the collisions between the robotic arm and an predefined area within the reachable workspace.

The Panda robotic arm already supports the implementation of such feature through their library "libfranka". In detail, the library offers the possibility of creating data structures called "VirtualWallCuboid"³. Such a structure is defined by four members. The first member is the virtual wall ID. The second member is the cuboid's corner Cartesian location, expressed in the base frame of the robotic arm. The third member is the transformation matrix, which could map the end-effector location and orientation from base frame to virtual wall frame such that the virtual wall is defined by the origin of its frame and the diagonal corner (i.e the second member of the VirtualWallCuboid). And the fourth, but not least, is a toggle parameter member that enables or disables the virtual wall during runtime. In conclusion, the "VirtualWallCuboid" could be used as a method to prevent any collision between the Panda robotic arm and the predefined area within its reachable workspace.

2.1.3 Safe mechanical interface

The usage of a robotic arm as an input device requires one or multiple point(s) of contact between the robotic arm and the operator. Within the scope of this assignment, a single point of contact is considered and it is located at the end-effector of the robotic arm and the wrist of the operator. This single connection between the robot and human should be made through a safe mechanical interface. This section details one such possible safe interface as reported by Hulin et al. (2008).



(a) The view of the connection between the hand of the human operator and the end-effector of the robotic arm when the two are in contact.

(b) The view of the hand of the human operator and the end-effector of the robotic arm when the two are not connected.

Figure 2.2: The magnetic clutch used as a handle by Hulin et al. (2008) in their human machine interface.

The interface is composed of two parts and a locking mechanism. The two components are:

- component 1 - attachable to the end-effector of the robotic arm.
- component 2 - attachable to the human wrist in order to leave the hand free for a future exoskeleton hand system that will provide the operator with a realistic sensation when for example grasping an object.

³https://frankaemika.github.io/libfranka/structfranka_1_1VirtualWallCuboid.html

The proposed type of the locking mechanism between the two parts is an electromagnetic clutch. The two friction surfaces are engaged by the attractive force between a permanent magnet and an electromagnet. Allowing the clutch to be locked when powered or when unpowered. Since either engaging or disengaging must require activation of the electromagnet resulting in a relatively large amount of energy required, this could result in a problem. As an alternative, the electromagnet can be replaced with a permanent magnet resulting in no power consumption and the loss of the ability to modulate the force required to separate the two friction surfaces (Plooij et al., 2015). In this case, the clutch must be designed so that it releases the user when the maximum applied forces and torques exceed the maximum force of the clutch. The attaching forces and torques of the clutch is defined by:

- the geometry of the clutch
- the arrangement of the magnets
- the strength of the magnets

Although the interface is an important part of a haptic input device, due to time constrained, the default Panda's gripper is used so that the focus of this assignment is not on designing and validating the interface between a human wrist and an end-effector of a robotic arm. The focus is rather on the safety and haptic usage of the Panda robotic arm in an overall system design.

2.1.4 Conclusion

In conclusion, the safety aspects covered by this sub-chapter aims at answering the first main research question:

"How can the Panda robotic arm be safely used in interaction with humans?"

In order to use the Panda robotic arm in interaction with humans, the control algorithm of Panda should include limitations on the power transferred from the controller to manipulator and on the total energy of the system, as well as contact force limitation and virtual walls. The power and energy limits that will be used in the design and implementation of the Panda's controller are summarized in Table 2.2. In case of crushing between a human and a robot, an appropriate index would be the contact force (Haddadin and Croft, 2016). This contact force should not exceed 140 N according to ISO/TS15066 (2016). The implementation will contain a limit of 140 N on the translational components of the force generated by the end-effector of the Panda robotic arm. Explicit limits for the rotational components of the force are not reported in literature to date, to the author's best knowledge. Therefore, no limit on the rotational force is applied as such, however, it is partially taken care of through the energy limit.

Another important part of guaranteeing safety during interaction is the human-robot interface discussed in section 2.1.3. Due to time limitation the development of such a safe interface is left out of the scope of this thesis. However, the virtual walls will be implemented through the Panda build-in software library such that the reachable workspace of the robotic arm can be restricted to comply with the safety standards.

2.2 Haptic interface aspects

2.2.1 The quality assessment of a haptic device

A haptic device is an actuated human-machine interface which measures the position and forces of the user that operates the device and provides force and torque feedback to the operator through the human sense of touch based on reacting forces and torques from objects in a real, teleoperated, or virtual environment (Srinivasan, 1995).

Haptic devices can either be force-feedback devices or tactile-feedback devices, depending on the level of feedback provided. Within this research, the Panda robotic arm will be used as a

force feedback device because it addresses the sensations felt by the muscles, joints, and tendons. Unlike the tactile-feedback devices that address the sensations felt by the skin, such as texture, temperature, and vibration. The force feedback device is used in a system to increase the level of immersion the user feels when performing a certain task. This is achieved by displaying forces from virtual or real remote environments to the user. End goal is to improve the task performance of the user.

A good haptic device typically depends on the specific application that is targeted for. Within the scope of this assignment, the specific application is not defined. However, a general application for haptic interactions with either virtual or remote environments is aimed at. Furthermore, Sun et al. (2017) highlights the most commonly listed properties of a haptic ground-based force-feedback device, together with their ideal qualitative values. They looked at the currently available haptic devices both on the market and in research labs. These properties (Table 2.4) are compared with the Panda robotic arm capabilities in the following section 2.2.2.

Performance criterion	Qualitative Ideal	Meaning
Degrees-of-freedom (DOF)	High	The number of orthogonal motions either permitted or driven by the device.
Workspace	High	The area or volume in real-world space that the end-effector can reach.
Isotropy	High	The uniformity of the end-effector moving in all generalized workspace directions.
Dexterity/ Manipulability	High	Quantification of the device's ease of arbitrarily changing position and orientation for a given posture.
Inertia	Low	The resistance felt by the user while moving the end-effector.
Friction	Low	Forces of resistance that oppose motion.
Stiffness	High	The ability of a device to mimic a solid virtual wall or object.
Input position resolution	High	The smallest change of position which can be detected by sensors.
Output force resolution	High	The smallest incremental force that can be generated by the device.
Operating bandwidth	High	The speed of response to a given excitation.
Peak force	High	The maximum force that the actuators of a device can generate over a very small time interval.
Continuous force	High	The force that the end-effector can exert for an extended period.
Peak acceleration	High	The ability of a device to simulate the impact with stiff virtual objects.

Table 2.4: The most common properties and their ideal qualitative values for haptic devices available both on the market and in research labs (Sun et al., 2017).

2.2.2 The Panda robotic arm

The aim of this section is evaluating the Panda robotic arm based on the most common physical performance requirements of high-performing haptic devices as discussed in section 2.2.1. The Table 2.5 presents the properties from Table 2.4 from the Panda robotic arm point of view.

Performance criterion	Qualitative Ideal	Panda robotic arm
Degrees-of-freedom (DOF)	High	7 DOF available (Figure 2.1).
Workspace	High	sphere like shape with a radius of 855 mm (Figure 2.3) and section 2.2.3 covers an in-depth analysis.
Isotropy	High	able to uniformly move during certain tasks as long as suitable initial joint positions are set to avoid the robotic arm reconfiguring its posture due to its joint limitations.
Dexterity/ Manipulability	High	Not evaluated.
Inertia	Low	Not evaluated.
Friction	Low	Not evaluated.
Stiffness	High	able to mimic the presence of virtual walls, however the documentation presents no value for defining its stiffness.
Input position resolution	High	the repeatability of the robotic arm task is ± 0.1 mm (EMIKA, 2018), which implies that this is also the detection limit of a change in position.
Output force resolution	High	Not evaluated.
Operating bandwidth	High	the control loop runs at 1 kHz.
Peak force	High	Not evaluated.
Continuous force	High	the values for each joint are available (Table 2.3).
Peak acceleration	High	information available only for the commanded end effector maximum acceleration in translational axis that is 13 m/s^2 and in the rotational axis that is 25 rad/s^2 . ⁴

Table 2.5: The most common properties and their ideal qualitative values for haptic devices (Sun et al., 2017) evaluated for Franka Emika Panda robotic arm.

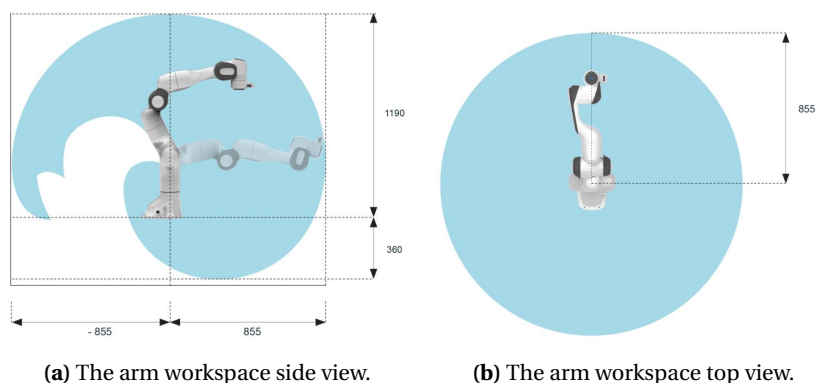


Figure 2.3: The workspace of the Panda robotic arm (all numbers are in mm) EMIKA (2018).

⁴Source: https://frankaemika.github.io/docs/control_parameters.html

2.2.3 The optimal workspace - performance criterion

An important performance criterion is the workspace. The performance of the haptic setup will not only depend on the workspace of the robotic arm but also on how it is interfaced with the human right-arm. Ideally, the workspace of the human right-arm should be fully covered by workspace of the robotic arm. One way would be evaluating various setups using a number of subjects, and another would be analyzing them using functional criteria. The latter was considered by Zacharias et al. (2010) when analysing the bimanual human-robot interface made by Hulin et al. (2008). This analysis uses the workspace model (Zacharias et al., 2007), which quantifies the workspace and includes not only the position that the robotic arm can reach, but also its orientation. Even if a point in space is reachable, certain tasks require also a specific orientation to be properly performed.

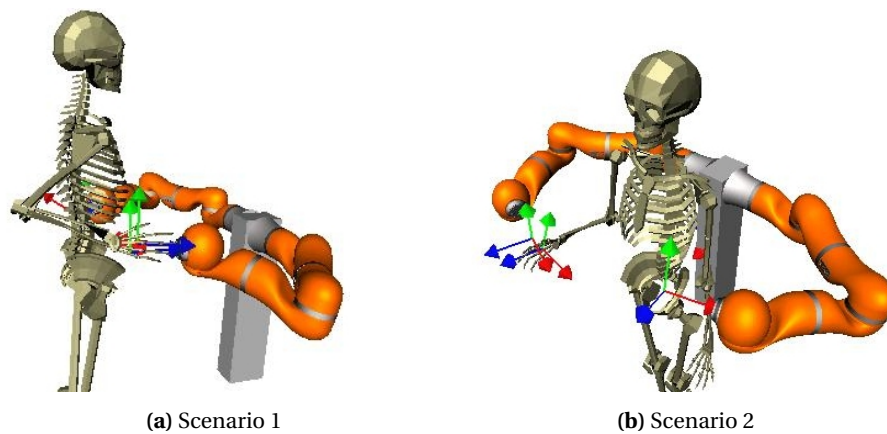


Figure 2.4: Setups considered for analysis of workspaces (Zacharias et al., 2010).

Zacharias et al. (2010) investigated two scenarios (Figure 2.4) for two cases to compare with: the whole and the restricted human workspace. The restricted human workspace consists of the area that humans most use in every day life, following experiments as reported by Howard et al. (2009). In each case, the robotic arm workspace was compared with the human workspace in terms of maximum coverage % and location of the human shoulder. In conclusion, the whole workspace of the human right-arm was covered by the robotic arm by 43% and 63%, in scenario 1 and 2, respectively. Moreover, for the restricted human workspace, the maximum coverage was 66.8% and 64.4%, in scenario 1 and 2, respectively. Although the scenario 1 scores a higher maximum coverage in the restricted human workspace, the scenario 2 is recommended to be implemented because the area of the region where the maximum coverage occurs is greater. Herein, the same ergonomic scenario 2 can be used for the Panda robotic arm setup. We can assume that this scenario is herein suitable, even if the setup investigated by Zacharias et al. (2010) has the DLR-KUKA LWR robotic arm with a sphere-like workspace shape of 936mm radius, because the Panda's workspace radius of 855mm is larger than the Dutch adult average arm length of 715mm (Dined, 2004).

2.2.4 The continuous force - performance criterion

The continuous force is the force that the end-effector can exert for an extended period of time. This value has been discussed from an safety point of view and now haptic performance is taken into account. It makes sense to relate this with the force capabilities of the user. Therefore, the section aims at answering the following secondary research question: *"How does the force safety limit applied to the Panda relates to the maximum force capabilities of a human arm?"*

During the literature review, no complete information was found that relates the maximum force a human right-arm outputs with the arm configuration within its workspace, in a general way. However, more commonly used in research is the maximum joint torques a human right-arm outputs (Carignan et al., 2005; Letier et al., 2008). A way to obtain the maximum forces from maximum joint torques is using the screw theory. Screw theory is a tool used in static and kinematic analysis of rigid bodies and mechanisms. The kinematic modelling of a robot manipulator describes the relationship between the links and joints that compose its kinematic chain. (Rocha et al., 2011; Stramigioli and Bruyninckx, 2001) To apply the screw theory, a model of the human arm is needed. Tondu et al. (2005) provides one that was used in designing an anthropomorphic robot-arm. The 7 degrees of freedom (DOF) model can be seen in Figure 2.5, in which the arm points towards the ground on the minus x-axis, parallel to the ground towards right on the minus y-axis and parallel to the ground forward on the minus z-axis. The same human right-arm model was also used by Zacharias et al. (2010). Table 2.6 summarizes the joint limits with the corresponding motion of body links in terms of external–internal rotation, flexion–extension, and abduction–adduction (Carignan et al., 2005) and the arm maximum torques extracted from (Table I in Letier et al. (2008)).

Joint	Name motion (Figure 2.5)	Range motion (°) (Carignan et al., 2005)	Maximum torques (Nm) (Letier et al., 2008)
1 (SA)	Shoulder abduction	134	134
	Shoulder adduction	-48	
2 (SF)	Shoulder flexion	188	115
	Shoulder extension	-61	
3 (AR)	Arm external (lateral) rotation	34	60
	Arm internal (medial) rotation	-97	
4 (EF)	Elbow flexion	142	72
	Elbow extension	0	
5 (PS)	Forearm pronation	85	9
	Forearm supination	-90	
6 (WA)	Wrist abduction	47	21
	Wrist adduction	-27	
7 (WF)	Wrist flexion	90	20
	Wrist extension	-99	

Table 2.6: The human right-arm joint limits, name and range of motion and maximum torques.

It is proven in (Stramigioli and Bruyninckx, 2001) that if the energy is exchanged only via the end effector (hand) and the joints, then it can be assumed through power continuity the following:

$$P_{\text{hand}} = W^{0,n} T_n^{0,0} = W^{0,n} J(\mathbf{q}) \dot{\mathbf{q}} = P_{\text{joints}} = \boldsymbol{\tau} \dot{\mathbf{q}} \quad (2.7)$$

where $T_n^{0,0}$ is the twist of body n with respect to body frame 0 expressed in body frame 0, $W^{0,n}$ is the wrench acting on body n expressed in body frame 0 and $J(\mathbf{q})$ is the Jacobian matrix. Moreover, equation 2.8 also holds.

$$\boldsymbol{\tau} = J^T(\mathbf{q})(W^{0,n}) \quad (2.8)$$

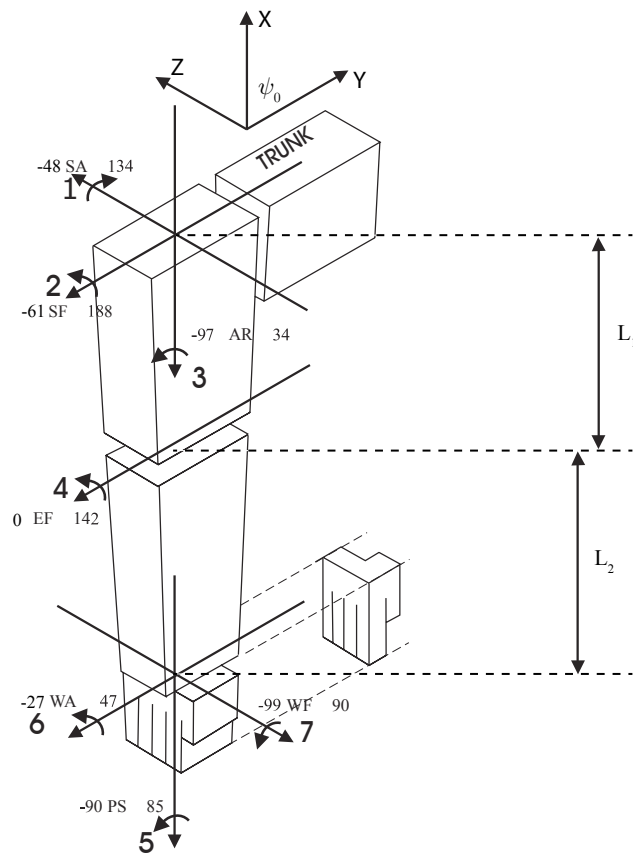


Figure 2.5: The human right-arm model joint frames. Joint limits differ from original Figure by Tondu et al. (2005). Where L_1 and L_2 are 0.20 m and 0.25 m, respectively.

Equation 2.8 can be used to relate the maximum torques from literature (Table I in Letier et al. (2008)) to the maximum force as part of the wrench ($W^{0,n} = [\tau_x, \tau_y, \tau_z, F_x, F_y, F_z]$) through the Jacobian matrix computed using screw theory (for details see Appendix A).

Firstly, to simplify the analysis, the F_x, F_y, F_z components of the maximum force exerted by the human right-arm on the workspace are considered independently, never more than one at a time, such that, for example, the F_x and F_y would be zero when considering F_z .

Secondly, the human hand joint space, 5^7 configurations were obtained by discretizing into 5 equal parts the motion range of each of the 7 joints (see Table 2.6). Thirdly, for each of the 5^7 joint configurations, when the torque obtained with a 1N wrench iteration from 0 to 400 N of equation 2.8 is less or equal than the maximum torque (Table 2.6), the force component of the wrench used for its computation is saved. The iteration runs until either the force or torque reach their threshold, i.e. 400N as reported by Das and Wang (2004) for the force and the values listed in Table 2.6 for the torque. The reported 400N threshold limit was obtain through user experiments in which the greatest pull strength was recorded for males and females participants in the seated and standing positions. The algorithm used to compute the maximum force capabilities of a human right-arm is available as pseudo-code (Algorithm 1) in Appendix A.2.

Lastly, since there may be more than one joint configuration that allows the human hand to reach a particular location, the workspace was also discretized. By choosing a 5 cm^3 area, 441 boxes were obtained, such that now a maximum force per box can be calculated. Since each joint configuration has its own corresponding force (according to equation 2.8), the workspace

discretization allows the final number of maximum forces considered to be reduced from 5^7 to 441. Moreover, these 441 points are on the surface of 5 discrete spheres of radius values 0.154 m, 0.272 m, 0.368 m, 0.429 m and 0.450 m. These radius values are obtained from equation A.3 (see Appendix A.1) that considers the human right-arm model shown in Figure 2.5 and all joint configuration angles.

Results and discussion

To answer the research question that this section addresses, the force exerted by a human right-arm and the literature reported 140N safety limit are compared. Firstly, the individual F_x , F_y and F_z components of the wrench are determined by iterating equation 2.8. This yields 5^7 values for each component. Secondly, the number of forces is reduced to 441 by discretizing the workspace. A histogram can now be used to show the frequency of the 441 values in bins of 0 - 140 N, 140 - 280 N and 280 - 420 N, that represent 100%, 200% and 300% of the force limit (Figure 2.6).

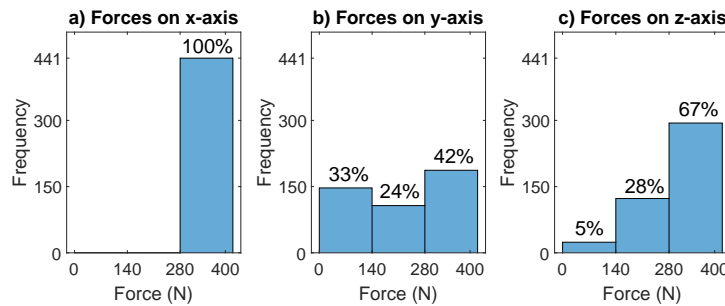


Figure 2.6: The histogram of the maximum force components F_x (a), F_y (b) and F_z (c) that the human right-arm can exert in the workspace.

The histogram shows that, the human right-arm acts with the maximum force F_x component (push-pull motion) on 100% of the workspace with a strength higher than 280 N (i.e. 200% of the safety force limit), while, on 57% and 33% of the workspace, it acts with a strength lower than 280 N with its F_y (left-right motion) and F_z component (up-down motion), respectively (Figure 2.6). In other words, from a safety perspective, the maximum force exerted by the human right-arm exceeds the 140N safety limit, on 100%, 66% and 95% of the workspace for the F_x , F_y and F_z components, respectively.

When the 5 discrete spheres of radius values 0.154 m, 0.272 m, 0.368 m, 0.429 m and 0.450 m are considered, the position of the forces that are lower than the safety limit always falls on the 0.429m and 0.450m radius spheres for the F_y component, and on the 0.450m radius sphere for the F_z component. Since a clear 3D illustration is not possible, Figure 2.7 shows a 2D-representation of a slice of the total human right-arm workspace on the YZ plane, corresponding to the top view of the human right-arm, at shoulder level. The slice thickness is 5 cm, as much as the box size used to discretize the workspace. Note that, herein, the human right-arm model allows forces to be exerted even in the otherwise naturally less accessible area depicted with grey in the figure, because the motion range limits of each joint do not consider the limitations provided by the presence of a human trunk when acting in combination in reality.

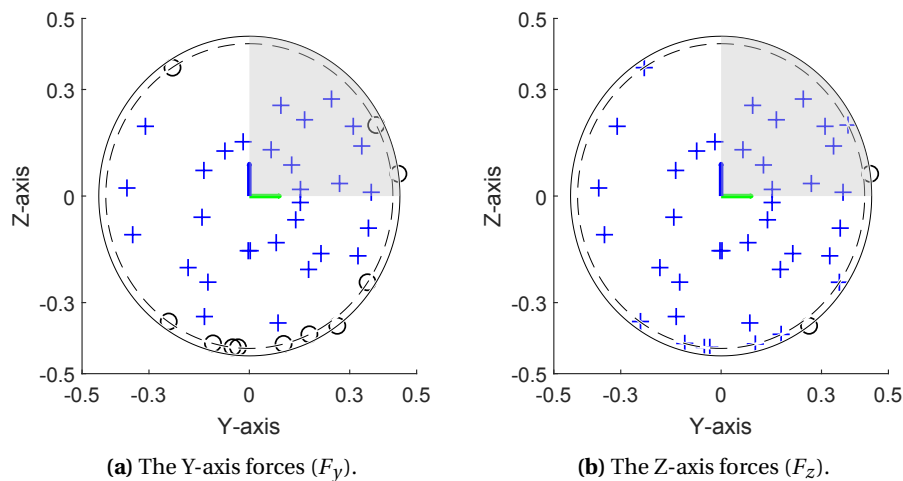


Figure 2.7: A slice of the human right-arm workspace in the YZ plane illustrating the location of the Y-axis(a) and Z-axis(b) maximum forces per 5 cm^3 box. The forces that have a magnitude higher or lower than the 140N safety force limit are represented by a cross(+) or a circle(o), respectively. The radius of the circles depicted are 0.429 m and 0.450 m for the dotted and straight line, respectively. The grey quarter circle represents the area behind the head, least accessible to a human arm under natural circumstances.

All in all, from a safety perspective, in most reachable workspace of the human right-arm, the user will be able to overcome the maximum force that the haptic device outputs.

2.2.5 Conclusion

The haptic aspects covered by this sub-chapter aim at answering the second main research question:

"How can the Panda robotic arm be effectively used as a haptic interface device?"

Although some performance criteria are not yet evaluated (Table 2.5, according to the available most common properties for haptic devices, the Panda robotic arm has the potential to be used as a haptic device. Out of all the performance criteria, the workspace and the continuous output force were investigated. Based on the work of Zacharias et al. (2010), the optimal Panda robotic arm workspace should be as illustrated in Figure 2.4b (Chapter 2.2.3), because the area of the region where the maximum coverage occurs is greater in scenario 2, compared with scenario 1, as explained in their article. Regarding the continuous force, the Panda robotic arm will be able to provide one third of the maximum force of the human right-arm within the reachable workspace. This is as good as any devices currently available on the market. Commercial devices are in the range of 3N to 20N, and for the research prototypes are in the range of 8N to 100N (Sun et al., 2017).

3 Design and implementation

In this chapter, the design and implementation of the robotic arm as haptic input device to be safely used by humans for telemanipulation is presented. First a state-of-the-art bilateral telemanipulation system is described. Next, the changes within the system architecture of the telemanipulation system required to allow the safe use of a Panda robotic arm as a master device are presented for both controllers, on the slave and master side. Three safety constraints are discussed: the energy limit and force limit on the slave side and the power limit on master side. Finally, the implementation of this system in ROS middleware is discussed for the slave and master controllers.

3.1 Current bilateral telemanipulation system

For the present project, the state-of-the-art telemanipulation system shown in Figure 3.1 was chosen as a model. It consists of a user being in physical contact with a master device in order to perform a certain task via the slave device located in a remote environment. The slave device needs to display the behaviour desired by the user performing the task, and the master device needs to accurately provide force feedback based on the interaction between the remote environment and the slave device. The user's performance of tasks relies on the controllers and communication channel, which are the connection between the master and slave devices.

The controllers situated in the channel must guarantee stability of the system and achieve high level of transparency, because transparency and stability are two important criteria in bilateral telemanipulation (Franken et al., 2011; Hashtrudi-Zaad and Salcudean, 2001; Lawrence, 1993).

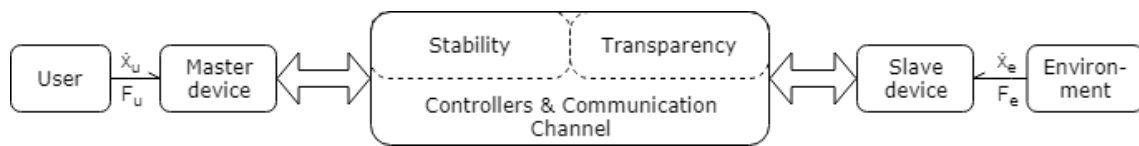


Figure 3.1: A current telemanipulation system overview.

In general, transparency is a performance measure of how well the complete system is able to convey to the user the perception of direct interaction with the environment (Lawrence, 1993; Hashtrudi-Zaad and Salcudean, 2001). Perfect transparency is technically achieved if the slave position and force are identical to the master position and force (Hashtrudi-Zaad and Salcudean, 2001). Therefore, the transparency layer contains a bilateral control algorithm to display the desired behaviour and obtain transparency. In the work of Nijhof (2018), transparency is obtained through an impedance controller located on the slave side. The impedance controller calculates the generalized force (the wrench W_s) in the reference frame based on the stiffness of the spatial spring and the relative difference in position and orientation between the end-effector of the master and slave devices.

Stability is the fundamental requirement for every control system (Hashtrudi-Zaad and Salcudean, 2001). In particular, for the bilateral telemanipulation systems, unless specially accounted for, stable behaviour is compromised in the presence of time-varying destabilizing factors such as hard contacts, relaxed user grasps, stiff control settings, and/or communication delays. In the current system (Nijhof, 2018), stability is achieved through implementation of passivity layers that preserves the system stability, even in the presence of time delays in the communication channel. The passivity layers ensure that no "virtual" energy is generated. It should be located on the slave side and the master side as described by Franken et al. (2011). However, it is not implemented in the final system because of time restrictions. The influence

of destabilizing factors such as network communication delays and energy generation due to discretization is expected to be minimal as high enough sampling frequency is assumed.

3.2 Panda haptic device within the bilateral telemanipulation system

The design of this project utilizes for the first time, a Panda robotic arm as a master device that complies with the required safety standards (Table 2.2). This requires changes within the system architecture to accommodate the three safety constrains: the energy limit and force limit on the slave side and the power limit on master side.

3.2.1 The slave side

For this project, the slave controller was designed based on previous work by Nijhof (2018). The modifications that accommodate the introduction of an energy and force limit to the system are done in the impedance controller, as can be seen in the signal flow diagram below (Figure 3.2). The energy and force limits are summarized in Table 2.2, as part of the analysis chapter conclusion.

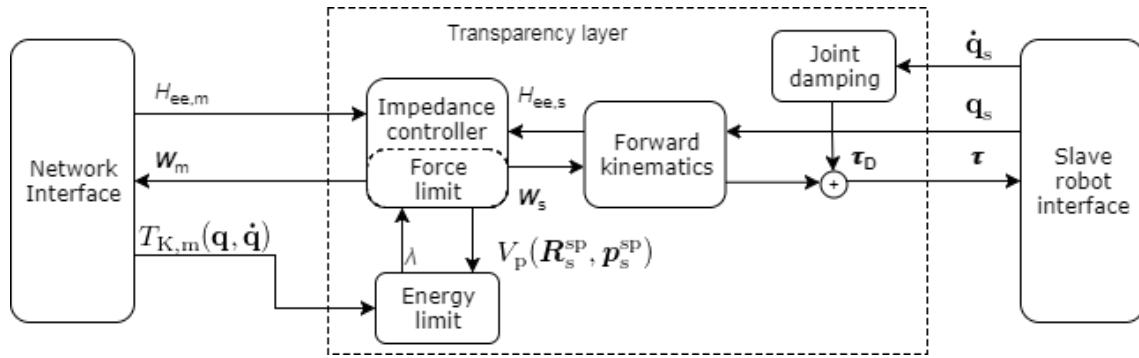


Figure 3.2: The slave design architecture. The bold symbols ($\mathbf{q}_s, \dot{\mathbf{q}}_s, \boldsymbol{\tau}, \boldsymbol{\tau}_D, \mathbf{W}_m, \mathbf{W}_s$) denote a vector.

The first modification (energy limit) was implemented as described by Tadele (2014) and Raiola et al. (2018). The total energy of the system is the sum of the kinetic energy of the master device, and the potential energy due to the spatial spring, defined as:

$$E_{\text{tot}} = T_{K,m}(\mathbf{q}, \dot{\mathbf{q}}) + V_p(\mathbf{R}_s^{\text{sp}}, \mathbf{p}_s^{\text{sp}}) \quad (3.1)$$

where the kinetic energy is calculated, on the master side, as:

$$T_{K,m}(\mathbf{q}, \dot{\mathbf{q}}) = \frac{1}{2} \dot{\mathbf{q}}^\top \mathbf{M}(\mathbf{q}) \dot{\mathbf{q}} \quad (3.2)$$

where the $\mathbf{M}(\mathbf{q})$ is the inertia matrix and $\dot{\mathbf{q}}$ is the joint velocity vector. Furthermore, the potential energy V_p stored in the spatial spring is composed of three components V_t, V_o, V_c representing the translational, rotational, and coupling components, respectively:

$$V_p(\mathbf{R}_s^{\text{sp}}, \mathbf{p}_s^{\text{sp}}) = V_t(\mathbf{R}_s^{\text{sp}}, \mathbf{p}_s^{\text{sp}}) + V_o(\mathbf{R}_s^{\text{sp}}) + V_c(\mathbf{R}_s^{\text{sp}}, \mathbf{p}_s^{\text{sp}}) \quad (3.3)$$

The potential energy (V_p) is defined in terms of the \mathbf{R}_s^{sp} and \mathbf{p}_s^{sp} , which together define the position and orientation of the relative configuration. The computation of these components (3.3) as defined in the work of Fasse (1997) and Stramigioli (2001) is:

$$\begin{aligned} V_t(\mathbf{R}_s^{\text{sp}}, \mathbf{p}_s^{\text{sp}}) &= -\frac{1}{4} \text{tr}(\tilde{\mathbf{p}}_s^{\text{sp}} \mathbf{G}_t \tilde{\mathbf{p}}_s^{\text{sp}}) - \frac{1}{4} \text{tr}(\tilde{\mathbf{p}}_s^{\text{sp}} \mathbf{R}_s^{\text{sp}} \mathbf{G}_t \mathbf{R}_s^{\text{sp}} \tilde{\mathbf{p}}_s^{\text{sp}}) \\ V_o(\mathbf{R}_s^{\text{sp}}) &= -\text{tr}(\mathbf{G}_o \mathbf{R}_s^{\text{sp}}) \\ V_c(\mathbf{R}_s^{\text{sp}}, \mathbf{p}_s^{\text{sp}}) &= \text{tr}(\mathbf{G}_c \mathbf{R}_s^{\text{sp}} \tilde{\mathbf{p}}_s^{\text{sp}}) \end{aligned} \quad (3.4)$$

where $\text{tr}()$ is the tensor trace operator, and \mathbf{G}_t , \mathbf{G}_o , \mathbf{G}_c are the translational, rotational, and coupling co-stiffness matrices respectively. The total energy limitation is achieved through regulating the amount of potential energy of the spatial spring. This is possible because the total energy of the system is direct proportional with the potential energy (eq. 3.1). As it can be observed, the potential energy components (3.4) are proportional to the co-stiffness matrices \mathbf{G}_x (for $x=t,o,c$). By limiting the co-stiffness matrices, the potential energy is also limited. The formula for the total initial system energy using the initial co-stiffness matrices \mathbf{G}_{x_i} is:

$$E_{\text{tot}_i} = T_{K,m}(\mathbf{q}, \dot{\mathbf{q}}) + V_{p_i}(\mathbf{R}_s^{\text{SP}}, \mathbf{p}_s^{\text{SP}}) \quad (3.5)$$

The actual co-stiffness matrices limiting is done by a factor λ :

$$\mathbf{G}_x = \lambda \cdot \mathbf{G}_{x_i} \quad \text{for} \quad x=t,o,c \quad (3.6)$$

where depending on the threshold E_{max} (see Chapter 2.1.1 and the safety limits in Table 2.2), λ is calculated as:

$$\lambda = \begin{cases} 1, & E_{\text{tot}_i} \leq E_{\text{max}} \\ \frac{E_{\text{max}} - T_{K,m}(\mathbf{q}, \dot{\mathbf{q}})}{V_{p_i}(\mathbf{R}_s^{\text{SP}}, \mathbf{p}_s^{\text{SP}})}, & \text{otherwise} \end{cases} \quad (3.7)$$

where E_{tot_i} and V_{p_i} are the initial total and potential energies respectively, calculated with the initial co-stiffness matrices \mathbf{G}_{x_i} . Therefore, the total energy of the system expressed as:

$$E_{\text{tot}} = T_{K,m}(\mathbf{q}, \dot{\mathbf{q}}) + \lambda \cdot V_{p_i}(\mathbf{R}_s^{\text{SP}}, \mathbf{p}_s^{\text{SP}}) \quad (3.8)$$

will always be less or equal than the desired threshold value E_{max} . Moreover, the impedance controller now takes into account the total energy in the system that is defined as the sum of the kinetic energy of the master device and the potential energy due to the spatial spring (Stramigioli, 1998).

The second modification (force limit) is implemented on slave side because the generalized force (i.e. wrench) of the spatial spring is computed here. In detail, the magnitude of the force component of the wrench expressed in end-effector frame is limited to the safe force (i.e. 140N). It is important that the two wrenches applied to the master and slave devices are equal in magnitude to keep the power continuity concept required for future implementation of the passivity layers (Franken et al., 2011).

Unlike the impedance controller, the other two components of the transparency layer (the forward kinematics and the viscous joint damping) were not modified.

The forward kinematics component contains two functionalities. A functionality translates joint positions (\mathbf{q}_s) to end effector position and orientation represented by a homogeneous matrix in reference frame with respect to reference frame ($H_{e,e,s}$). And the other functionality translates a wrench (\mathbf{W}_s), applied to the end effector expressed in reference frame, to joint torques, applied on individual joints of the KUKA LWR 4+.

The viscous joint damping is part of the control actions for the KUKA LWR 4+. The damping is performed on joint velocity ($\dot{\mathbf{q}}_s$) available from the robot interface and follows equation 3.9.

$$\boldsymbol{\tau}_D = -D_j \dot{\mathbf{q}}_s \quad (3.9)$$

To sum up, the designed and implemented slave system architecture is presented in Figure 3.2. The network interface and slave robot interface, as well as the transparency layer that mediates between them is shown. The signal paths are represented by arrows, both outside and inside the transparency layer, which contains the component that was modified (the impedance controller) as described above, and the two components that were used as such (the forward kinematics and the joint damping).

3.2.2 The master side

On the master side, a transparency layer was created between the network interface and the master robot interface, as described in Figure 3.3. The safe operation of the Panda robotic arm is a main objective of the presented work. Therefore, the transparency layer on the master side was carefully designed and implemented such that the power variable (P_{c_m}) is limited and the kinetic energy ($T_{K,m}$) is transferred over the network to the slave side, where the total energy is limited.

In detail, the power flowing from the controller to the master device is monitored to not exceed the power limit set according to safety limits (Table 2.2). This power limitation approach has been presented by Raiola et al. (2018) and follows the research of Tadele (2014). If an initial damping matrix $\bar{\mathbf{B}}_i$ is chosen in joint space, the power from the controller is expressed as:

$$P_{c_i} = \underbrace{(\mathbf{J}^\top(\mathbf{q})(\mathbf{W}_m)^\top - \bar{\mathbf{B}}_i\dot{\mathbf{q}})^\top \dot{\mathbf{q}}}_{P_{c_m}} + \underbrace{\hat{\mathbf{G}}(\mathbf{q})\dot{\mathbf{q}}}_{P_{c_g}} \quad (3.10)$$

where $\mathbf{J}(\mathbf{q})$ is the manipulator Jacobian that maps joint velocities with generalized velocities (Stramigioli and Bruyninckx, 2001); $\hat{\mathbf{G}}(\mathbf{q})$ is the gravity compensation; $\dot{\mathbf{q}}$ is the joint velocity vector; \mathbf{W}_m is the wrench calculated on the slave side; P_{c_m} is the power consumed for providing the force-feedback to the operator and P_{c_g} is the power consumed for gravity compensation. The P_{c_m} is the power that needs to be limited in case of an uncontrolled collision. This is done through adjusting the initial damping with a scaling term β :

$$\bar{\mathbf{B}} = \beta \cdot \bar{\mathbf{B}}_i \quad (3.11)$$

using the threshold values P_{\max} (Table 2.2), the scaling term β is defined as:

$$\beta = \begin{cases} 1, & P_{c_m} \leq P_{\max} \\ \frac{(\mathbf{J}^\top(\mathbf{q})(\mathbf{W}_m)^\top)^\top \dot{\mathbf{q}} - P_{\max}}{\dot{\mathbf{q}}^\top \bar{\mathbf{B}}_i \dot{\mathbf{q}}}, & \text{otherwise} \end{cases} \quad (3.12)$$

Moreover, with respect to the kinetic energy ($T_{K,m}(\mathbf{q}, \dot{\mathbf{q}})$) of the master device, its value is calculated using equation 3.2 before it is being transferred over the network to be included in the limitation applied to the total energy (equation 3.8).

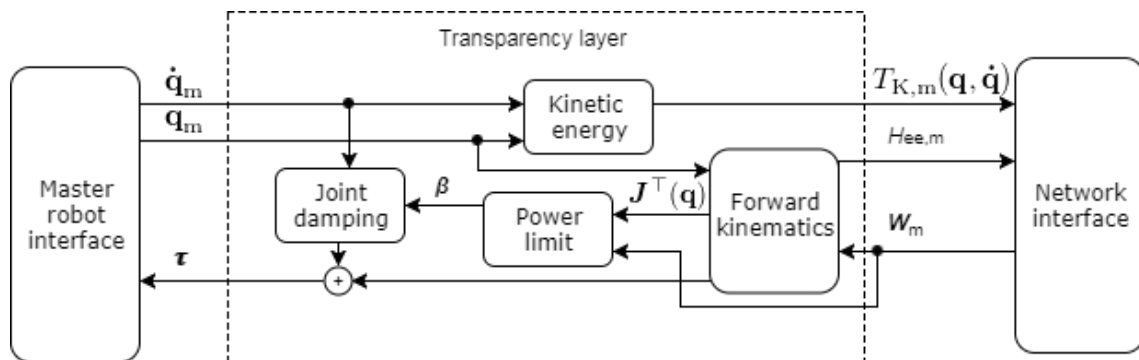


Figure 3.3: The master design architecture. The bold symbols ($\mathbf{q}_s, \dot{\mathbf{q}}_s, \boldsymbol{\tau}, \mathbf{W}_m$) denote a vector.

3.3 Implementation in ROS

The implementation of the designed teleoperation system is done in the Robot Operating System (ROS) middleware¹. The three main reasons for using this middleware are: widely usage in

¹Source: <http://www.ros.org/>

robotic research, official supported interface for the Panda robotic arm and familiarity with the ROS concepts. Firstly, the high popularity of ROS in robotics developed a strong community that helped it to mature on a software level. Therefore, a stable implementation is possible if the official guidelines are followed. Secondly, the Panda robotic arm comes with support for ROS through "franka_ros" package². And thirdly, the familiarity with the middleware is desired such that the implementation is completed within the limited time assigned for this project.

For this project, the master and slave controllers are implemented separately such that compiling and running the software code can be done on separate computational units.

3.3.1 The slave controller

For the controller implementation of the slave architecture design (Figure 3.2) two choices are worth mentioning: the interface connection of the slave robot and the software writing approach.

First, a KUKA LWR4+ model, simulated in the gazebo physics engine, is chosen to connect to the slave robot interface such that the system can be tested before involving the real hardware. The chosen model is created by the researchers at Research Center E. Piaggio at the University of Pisa, Italy³. This model can be viewed as a kinematic model, consisting of link lengths and joint configurations, combined with a dynamic model, consisting of parameters like link dimensions, inertia and joint friction and damping parameters. Regarding the accuracy of the model parameters, no detailed investigations are made. The mass properties are assumed realistic enough based on the mass distribution and the total mass of the links. However, idealized settings are used for the static friction and viscous damping parameters at 0.01 (Nm) and 0.01 (Nm/s/rad), respectively. Values follow previous work done by Teeffelen (2018).

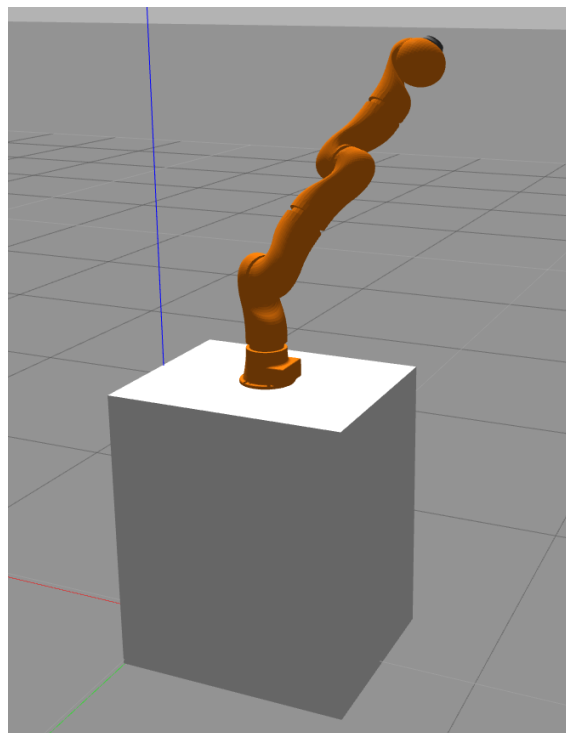


Figure 3.4: The KUKA LWR4+ model simulated in Gazebo.

Second, the chosen approach of writing the software follows the guidelines by Ellery (2017) to generate computational general components. The aim of using the general components ap-

²Source: https://github.com/frankaemika/franka_ros

³The model is available on their GitHub: <https://github.com/CentroEPiaggio/kuka-lwr>

proach was to structure the software such that each general component is reusable. Towards this end, two general components, previously created by Nijhof (2018), are used: forward kinematics and impedance controller. First, the forward kinematics component was used without a change as no change was necessary. Second, the impedance controller component was updated to include the total energy limit when computing the generalized force for the master and slave devices ($\mathbf{W}_m, \mathbf{W}_s$), as covered in chapter 3.2.

3.3.2 The master controller

For the controller implementation of the master architecture design (Figure 3.3) three functionalities are included, for testing purposes: (1) the ability to enable and disable the force feedback received from the slave side, (2) the ability to enable and disable the virtual wall (as discussed in chapter 2.1.2) and (3) the ability to set force and torque thresholds for collision behavior (as discussed in chapter 2.1.2).

All functionalities are implemented as ROS service calls and are triggered during runtime through a command line in a terminal of the bilateral telemanipulation system. The first functionality is required because force feedback is generated during the starting of the system due to slave end-effector not matching the master end-effector position and orientation. Therefore, the system is initialized with the force feedback disabled and after a few seconds, it can be manually activated. The second functionality follows the reasoning from chapter 2.1.1 and is implemented using the official library "libfranka" that offers the ability to create a "VirtualWallCuboid" ⁴. The properties of the "VirtualWallCuboid" are predefined in the master's controller source code since these do not change during runtime. However, the validation of the implemented VirtualWallCuboid was not possible because, while Franka Control Interface does provide a way to retrieve the properties of the defined virtual walls, ensuring such the existence of the walls within the software, there is no restriction applied on the end-effector of the Panda robotic arm. The third functionality is required to allow the user to interact with the Panda without triggering collision errors as explained in chapter 2.1.2. The default values are too low and higher values are set to avoid undesired interruptions.

⁴Source: https://frankaemika.github.io/libfranka/structfranka_1_VirtualWallCuboid.html

4 Evaluation

In this chapter, for the evaluation of the implemented design, a transparency (haptic performance) test and three safety (energy, power and force limit) tests are presented, after a short summary of the experimental setup and methods common to all these tests.

4.1 General setup and methods

For testing interactions between the user and objects in a remote environment, a virtual wall is generated in the Gazebo environment, at 2 cm distance from the box supporting the slave device, on a plane parallel to the YZ of the chosen reference frame. The master device used is the actual Panda robotic arm, while the slave device is only a simulation performed in Gazebo of the KUKA LWR 4+ robotic arm, due to time constraints. The PC used is an Intel i7 @ 2.8GHz x 8, with 12GB RAM, running a Linux with PREEMPT_RT patched kernel (i.e. 4.14.52-RT34) with Ubuntu 16.04 as operating system and the ROS Kinetic as middleware.

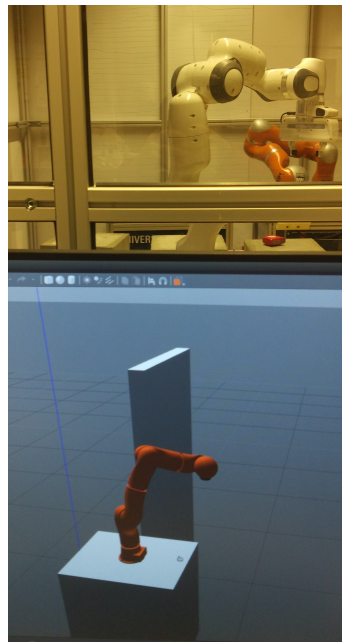


Figure 4.1: The Panda robotic arm (top, real hardware) and the KUKA LWR 4+ robotic arm (bottom, simulated model) setup used during the transparency test (haptic performance test) and the three safety tests.

In all the evaluation tests performed, the master and slave device had a similar starting joint configurations (see Figure 4.1) that took into consideration the respective range of motion limits (KUKA Roboter GmbH, 2012; EMIKA, 2018). With respect to the master device, the boundaries for the force applied by a user to the robotic arm are set at 80 N and 100 N for contact and collision boundary, respectively. Contact is registered as long as the force and torque are within the boundaries and collision is registered whenever they exceed the upper threshold. After collision, a reset is needed before the robotic arm can resume its function. With respect to the slave device, within the transparency layer, the control and frequency parameters are set for the impedance controller as shown in Table 4.1, following previous work (Nijhof, 2018). All stiffness matrices are set to identity matrices multiplied with corresponding spring constants. The translational spring constant (k_t) of 500 N/m is used, while the orientation spring constant (k_o) is 50 Nm/rad. In both cases, too high spring constants would result in unstable behaviour and too low values would result in high errors between set-point and measured po-

sition and orientation of the end-effector. Coupling between commanded motion in rotation and translation domain is not used, therefore the coupling stiffness (k_c) is set to zero. The joint damping (D_j) is empirically determined to smooth the output torques given the impedance controller settings and the typical commanded motion. The same joint damping value (D_j) is used in computing the commanded torques for both the master and slave device. Moreover, the frequency of the communication network middleware ROS (f_{ROS}) matches the impedance controller frequency (f_{ctrl}) at 1 kHz.

Parameter	Value	Unit
f_{ctrl}	1	kHz
f_{ROS}	1	kHz
k_t	500	N/m
k_o	50	Nm/rad
k_c	0	N/rad
D_j	5	Nms/rad

Table 4.1: The controller parameters.

The evaluation considers four tests, namely, haptic, energy limit, power limit and force limit. For all of these, a set energy, power and force limit is used as shown in Table 4.2. The haptic test uses the same limits discussed in Analysis (section 2.1). However, the safety tests have different limits compared to the values established in Analysis, such that there is a different E_{max} value set for the energy limit test, a different P_{max} value set for the power limit test, and a different F_{max} value set for the force limit test.

	Energy (J)	Power (W)	Force (N)
Analysis	4.5	198	140
Test 1 -haptic performance	4.5	198	140
Test 2 - energy limit	3.5	198	140
Test 3 - power limit	4.5	5	140
Test 4 - force limit	4.5	198	30

Table 4.2: The energy, power and force limits set for each test and discussed in Analysis.

Although all three safety tests have always three limits set (i.e E_{max} , P_{max} , and F_{max}), the constraints are being validated one at a time. The energy, power and force are related also by the stiffness of the spacial virtual spring, joint velocity and the inertia matrix (see Chapter 3). If the limit is validated, the method can then be applied for any other limit values. A constrain value chosen for validation must satisfy the following two conditions: (1) be as much as the value shown in Analysis or lower, and (2) be the first to reach its maximum among all three limits set. Therefore, the values are chosen (see Table 4.2) such that the experiments would not be tiring for the user, and such that they are the first limit reached.

4.2 Test 1 - A transparency test - The haptic performance

4.2.1 Goal

The two goals of this test are (1) to validate that the end-effector of the slave follows that of the master device and (2) to validate that a proper force feedback is established between them. For the first goal, the Cartesian position and orientation of the end-effector of each of the two robotic arms is evaluated and the error between them is determined. For the second goal of this test, the force of the user applied to the virtual wall remotely, and vice-versa, is plotted and discussed.

4.2.2 Method

First and foremost, for initialization (P0) three safety limits are set: 4.5J for the maximum total energy that may be allowed between the master and slave devices; 198W for the maximum power allowed between the master and user; and 140N for the force allowed between the master and user. Then, while viewing on a screen the slave device simulated in Gazebo environment where there is also a wall, the user moves the master end-effector slowly such that the slave end-effector can be seen approaching the virtual wall on the screen during an approximately 5 second free motion (P1). When the slave end-effector reaches the wall, the user continues to move the master end-effector for approximately 3 more seconds (P2) before moving it back to its initial position and approaching the wall location again (P3). The user repeats the interaction two more times with the wall for reproducibility (P4 and P6).

For this test, the Cartesian position and orientation of the end-effector of each of the two robotic arms is evaluated and the force feedback is validated as follows:

1) For the position, the error vector (\mathbf{e}_t) is computed by subtracting from the master position vector the slave position vector. The position error $\|\mathbf{e}_t\|$ is computed as the norm of the position vector. The mean and the standard deviation are then calculated for each individual part, as well as for the two performed motions: free motion (P1,P3 and P5) and wall restricted motion (P2,P4 and P6).

2) For the orientation, the error vector ($\tilde{\phi}(\tilde{R})$) is defined by the angle difference between the master (R_m) and slave (R_s) frame of the end-effectors. It is computed using the equation 4.1 (equation 29 from (Campa and De La Torre, 2009)). The orientation error $\|\mathbf{e}_o\|$ is computed as the norm of the orientation angle vector ($\tilde{\phi}(\tilde{R})$).

$$\tilde{\phi}(\tilde{R}) = \frac{1}{2} \begin{bmatrix} \tilde{r}_{32} - \tilde{r}_{23} \\ \tilde{r}_{13} - \tilde{r}_{31} \\ \tilde{r}_{21} - \tilde{r}_{12} \end{bmatrix} \in \mathbb{R}^3, \quad (4.1)$$

where \tilde{r}_{ij} is the ij -th element of \tilde{R} defined as the error rotation matrix expressing the relative orientation from the master (R_m) to slave (R_s) with respect to reference frame (equation 28 from (Campa and De La Torre, 2009)):

$$\tilde{R} = R_m R_s^T \quad (4.2)$$

Again, the mean and the standard deviation are then calculated for each individual part, as well as for the two performed motions: free motion (P1,P3 and P5) and wall restricted motion (P2,P4 and P6).

3) For the force feedback, the difference between the wrench exerted by the user on the master device end-effector (W_{in} , input force and torque) and the one exerted by the master device end-effector on user (W_m , output force and torque) is computed. The former is provided by the master device interface that uses the torque sensors of each joint to compute the estimated external wrench (force, torque) acting on the end-effector frame, expressed relative to the reference frame; while the latter, is computed by the impedance controller using the spatial spring stiffness parameters and the error in position and orientation of the master and slave end-effectors. As before, the mean and the standard deviation are then calculated for each individual part, as well as for the two performed motions: free motion (P1, P3 and P5) and wall restricted motion (P2, P4 and P6).

4.2.3 Expected results

The position and orientation of the end-effector of each of the two robotic arms is expected to be identical (minimal error) during free motion (P1, P3 and P5) and significantly different (larger error) during wall contact (P2, P4 and P6). Also, a proper force feedback should be es-

tablished between the two robotic arms and reflected by an similar plot of the input wrench (W_{in}) and the output wrench (W_m) against time.

4.2.4 Results and discussion

The position and orientation of the end-effector of each of the two robotic arms are closely overlapping during free motion (P1, P3 and P5), with errors of 0.026m and 0.075 rad or less, and significantly different during wall contact (P2, P4 and P6), with much larger errors that reach 0.074 m and 0.090 rad (see Figure 4.2). The mean and standard deviation values for each case are summarized in Table 4.3. Between the free motion and wall contact parts of the test, the mean for the position is much smaller in the former than the latter, as expected, since the impedance controller in the latter case is acting as a spring with one fixed extremity. The same holds true for the mean of the orientation error (see Figure 4.3). The total duration of the free motion (P1, P3 and P5) adds up to 11.1 seconds, while the interaction with the wall (P2, P4 and P6) is 8.07 seconds.

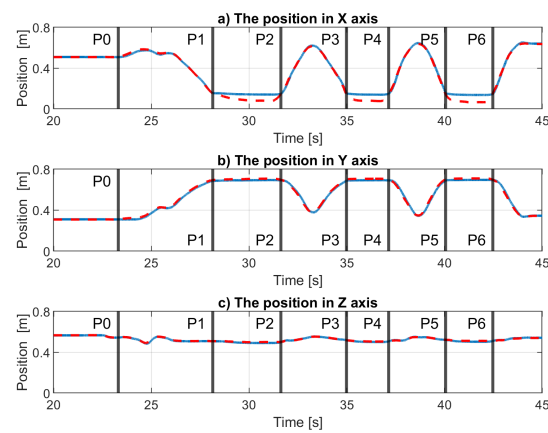


Figure 4.2: The position in X(a), Y(b) and Z(c) of the master (dashed, red) and slave (full, blue) end-effectors during free motion (P1, P3 and P5) and wall restricted motion (P2, P4 and P6).

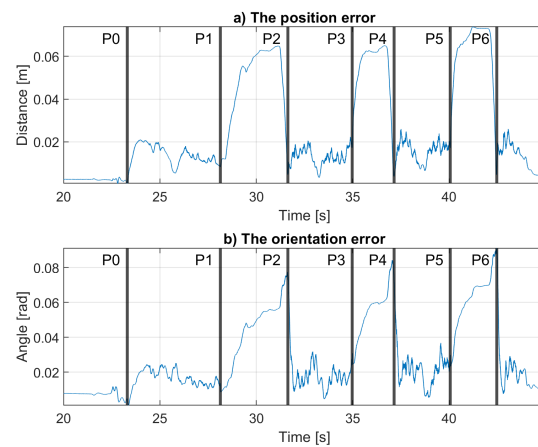


Figure 4.3: The position(a) and orientation(b) error between the master and slave end-effectors during free motion (P1, P3 and P5) and wall restricted motion (P2, P4 and P6).

Also, a proper force feedback is indeed established between the two robotic arms. For both the force (Figure 4.4) and the torque (Figure 4.5) of the action and reaction between the user and master device, a good overlap can be seen. During the interaction with the wall (P2, P4 and P6), the force feedback is significantly higher on the X axis compared to the Y and Z axis (Figure 4.4). This behaviour is due to the fact that the wall is parallel to the YZ plane of the Cartesian reference frame. While, the torque feedback is almost null on the X axis and reaches its highest and lowest values on the Y and Z axis (Figure 4.5), respectively. This behaviour is again related to the wall's location, which hinders the rotation of the KUKA end-effector around the Y and Z axis.

During the free motion (P1, P3 and P5), the force and torque are non-zero, as expected, because a complete dynamic compensation was not implemented for both slave and master. A thorough compensation would have to account for inertia, friction, gravity and Coriolis forces. However, herein, only the gravity ($\hat{G}(q)$, see section 3.2.2) and Coriolis compensations were considered as both were available through the Panda's build-in software library¹. Therefore, the user feels a resistance from the uncompensated dynamics of the devices involved in the interaction with the simulated environment.

¹Source: <https://frankaemika.github.io/libfranka/>

For the whole time (P1-P6), the difference between the input force/torque vector of the user and the output force/torque vector of the Panda (Figure 4.6) is calculated. The minimum, maximum, mean and standard deviation for each part is summarized in Table 4.4, below. The non-zero difference in forces is proportional to the acceleration of the Panda's end-effector and it is expected to be non-zero because the experiment involved moving the end-effector at non-constant velocity.

The mean of the force and torque differences during free motion (P1, P3 and P5) is $4.0 \pm 2.0\text{N}$ and $2.7 \pm 1.1\text{Nm}$ respectively; and during the wall restricted motion (P2, P4 and P6) it is $3.2 \pm 1.5\text{N}$ and $2.6 \pm 1.0\text{N}$, respectively. The similar values observed between the free motion and wall restricted motion indicates that the system in providing force and torque feedback with consistency.

Overall, the test results are as expected.

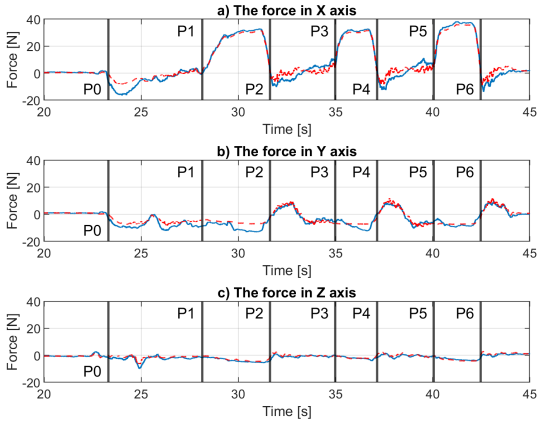


Figure 4.4: The force in X(a), Y(b) and Z(c) of the input force (full, blue) of the user and the opposite sign output force (dashed, red) of the Panda during free motion (P1, P3 and P5) and wall restricted motion (P2, P4 and P6).

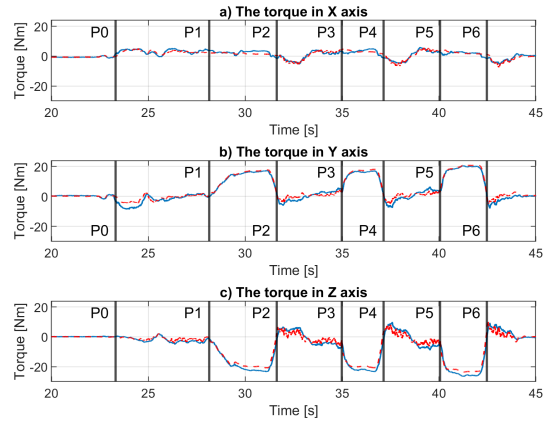


Figure 4.5: The torque in X(a), Y(b) and Z(c) of the input torque (full, blue) of the user and the opposite sign output torque (dashed, red) of the Panda during free motion (P1, P3 and P5) and wall restricted motion (P2, P4 and P6).

	Position error ($\ \mathbf{e}_t\ $) (m)				Orientation error ($\ \mathbf{e}_o\ $) (rad)			
	Min	Max	Mean	Std. Dev.	Min	Max	Mean	Std. Dev.
P1	0.001	0.021	0.014	0.004	0.001	0.025	0.017	0.005
P3	0.003	0.022	0.013	0.004	0.005	0.075	0.019	0.010
P5	0.004	0.026	0.016	0.005	0.006	0.075	0.022	0.011
Free motion (P1,P3,P5)	0.001	0.026	0.014	0.004	0.001	0.075	0.019	0.009
P2	0.005	0.065	0.048	0.018	0.009	0.078	0.044	0.018
P4	0.004	0.065	0.055	0.014	0.024	0.084	0.056	0.014
P6	0.005	0.074	0.063	0.015	0.023	0.090	0.062	0.015
Wall restricted motion (P2,P4,P6)	0.004	0.074	0.055	0.017	0.009	0.090	0.053	0.018

Table 4.3: The minimum, maximum, mean and standard deviation of the position and orientation errors between the master and slave end-effectors during free motion (P1, P3 and P5) and wall restricted motion (P2, P4 and P6).

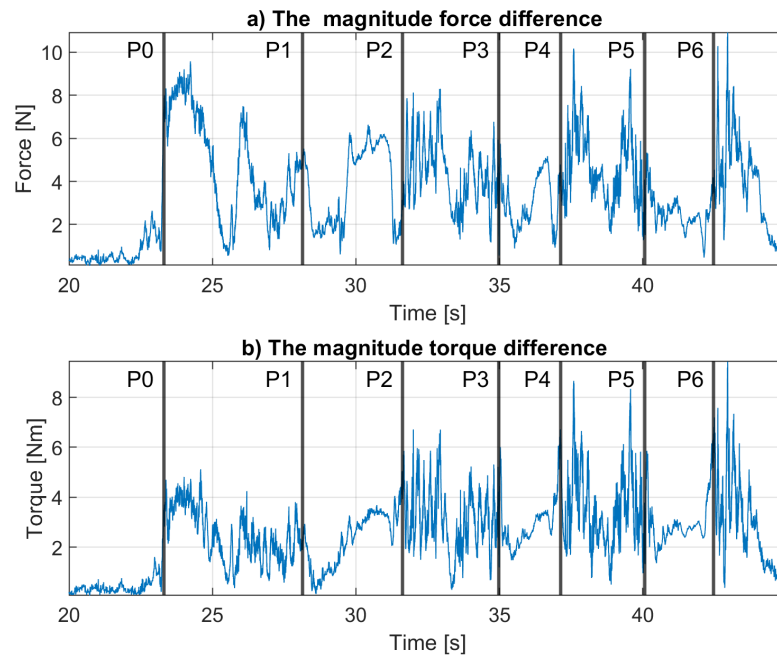


Figure 4.6: The magnitude force/torque of the difference between the input force/torque vector of the user and the output force/torque vector of the Panda.

	Force (N)				Torque (Nm)			
	Min	Max	Mean	Std. Dev.	Min	Max	Mean	Std. Dev.
P1	0.549	9.578	4.662	2.419	0.356	5.119	2.433	1.029
P3	1.165	8.301	4.333	1.431	0.287	6.713	3.050	1.228
P5	1.270	10.168	4.543	1.655	0.498	8.659	3.400	1.439
Free motion (P1,P3,P5)	0.549	10.168	4.073	2.041	0.287	8.659	2.745	1.113
P2	0.609	6.633	3.772	1.830	0.117	5.035	2.318	1.087
P4	0.554	5.752	3.029	1.195	1.188	6.716	2.920	0.973
P6	0.460	5.337	2.534	0.761	1.318	6.543	2.945	0.930
Wall restricted motion (P2,P4,P6)	0.460	6.633	3.206	1.515	0.117	6.716	2.665	1.057

Table 4.4: The minimum, maximum, mean and standard deviation of the difference between the input force/torque vector of the user and the output force/torque vector of the Panda, during free motion (P1, P3 and P5) and wall restricted motion (P2, P4 and P6).

4.3 Test 2 - A safety test - The energy limit

4.3.1 Goal

The goal of this test is to validate the energy limit (E_{\max}) set for a safe human handling of the Panda robotic arm as a haptic input device.

4.3.2 Method

To validate the energy limit, the total energy of the system (eq. 3.1 in Chapter 3) defined as the sum of the kinetic energy of the master device, and the potential energy due to the spatial spring should either be lower or equal with E_{\max} or else, a factor term (λ) is used to reduce the computed wrench (W_p) applied to the user by the Panda robotic arm.

Similar to the first test, for initialization (P0) two safety limits are set: 198W for the maximum power allowed between the master and user; and 140N for the force allowed between the master and user. And unlike the first test, for the safety limit herein tested, 3.5J is set as the maximum total energy that may be allowed between the master and slave devices, in order to reduce the effort required by the user to reach the limit during the experiment.

While viewing on a screen the slave device simulated in Gazebo environment where there is also a wall, the user moves the master end-effector slowly such that the slave end-effector can be seen approaching the virtual wall on the screen during free motion (P1). When the slave end-effector reaches the wall, the user continues to move the master end-effector (P2) before moving it back to its initial position and approaching the wall location again (P3). The user repeats two more times the interaction with the wall for reproducibility (P4, P5 and P6).

4.3.3 Expected results

At the beginning (P0) of the experiment, both the master and slave end-effectors have identical starting configurations and are not in motion. Therefore, the total energy of the system (see equation 3.1) is expected to be zero due to the potential energy (see equation 3.3) and kinetic energy (see equation 3.2) being zero. During the interaction with the wall (P2, P4 and P6), the total energy is expected to exceed the E_{\max} value and, as a result, the wrench feedback should be limited accordingly for the same time periods (P2, P4, P6).

4.3.4 Results and discussion

The total energy of the system is found to be not zero, but -75 J (Figure 4.7a), given the controller parameters chosen ($\mathbf{K}_t = 500\mathbf{I}$; $\mathbf{K}_o = 50\mathbf{I}$; $\mathbf{K}_c = 0\mathbf{I}$). Therefore, the output force and torque are not restricted, and user safety is not guaranteed as such. In detail, the total energy value is calculated to be -75 J due to the orientation component of the total energy potential (equation 3.4). Assuming identical configurations (i.e. $\mathbf{R}_s^{\text{SP}} = \mathbf{I}$; $\mathbf{p}_s^{\text{SP}} = \mathbf{0}$) and eq. 3.4, eq. 4.3 holds.

$$\begin{aligned} V_t(\mathbf{R}_s^{\text{SP}}, \mathbf{p}_s^{\text{SP}}) &= 0 \\ V_o(\mathbf{R}_s^{\text{SP}}) &= -\text{tr}(\mathbf{G}_o \mathbf{R}_s^{\text{SP}}) = -75 \\ V_c(\mathbf{R}_s^{\text{SP}}, \mathbf{p}_s^{\text{SP}}) &= 0 \end{aligned} \quad (4.3)$$

where $\text{tr}()$ is the tensor trace operator that computes the sum of the diagonal elements; \mathbf{R}_s^{SP} is the rotation matrix from the frame orientation of the master end-effector to the one of the slave end-effector; \mathbf{p}_s^{SP} is the position vector between the location of the master end-effector to the one of the slave end-effector; and \mathbf{G}_o is the rotational co-stiffness matrix computed from the rotational stiffness matrix (\mathbf{K}_o) by eq. 4.4.

$$\mathbf{G}_o = \frac{1}{2} \text{tr}(\mathbf{K}_o) \mathbf{I} - \mathbf{K}_o = 25\mathbf{I} \quad (4.4)$$

Therefore, the value is to be considered as an offset determined by the way the rotational potential energy is defined in the original formula itself (Tadele, 2014; Raiola et al., 2018). As it is,

the implemented energy safety limit can not be validated. The computed total energy is significantly higher than -75J during the interaction with the virtual wall (P2, P4 and P6) but values are always too low to ever trigger the energy safety limit (E_{\max}), which is set to 3.5J . The exact cause of the deviation was not explored in this study due to time restrictions.

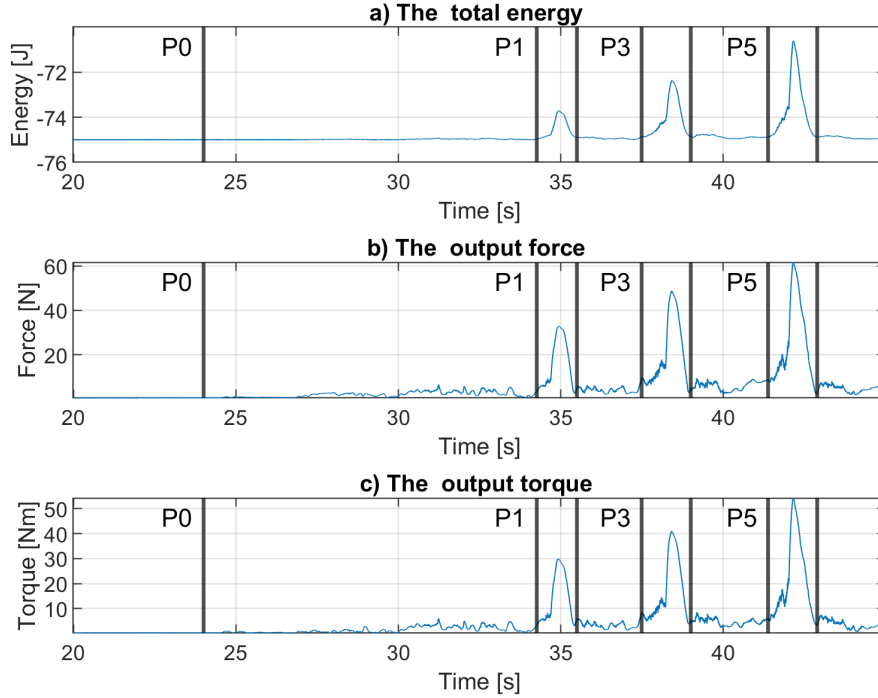


Figure 4.7: The system behaviour using the original formula (eq. 3.4) for computing the potential energy of the spatial spring. The total energy system (a); the magnitude force (b) and torque (c) output of the master device. The free motion parts are illustrated (P1, P3 and P5) within the figure, while the interaction with the wall (P2, P4 and P6) are not label within the figure.

A simple way to deal with the offset could be including it in the rotational potential energy ($V_o(\mathbf{R}_s^{\text{sp}})$) computation by adding a constant value computed from the controller parameter chosen (equation 4.5).

$$V_o(\mathbf{R}_s^{\text{sp}}) = -\text{tr}(\mathbf{G}_o \mathbf{R}_s^{\text{sp}}) + \text{tr}(\mathbf{G}_o) \quad (4.5)$$

Note that, all signals monitored during the wall interaction P2, P4 and P6 (i.e. the total energy, stiffness factor, force and torque as computed from the impedance controller) have a noisy peak as shown in Appendix B (see figures B.2 and B.1). The noisy instances occur when the stiffness parameters of the impedance controller are constantly updated to reduce the output force and torque. To clean the signals a 5-term moving average filter was applied.

The filtered results give a total energy as depicted in Figure 4.8. Both the force and the torque are limited during the wall interaction once the total maximum energy (E_{\max}) is exceeded (see Table 4.5). When the computed total energy exceeds the E_{\max} set, the force magnitude does not exceed 58N (Figure 4.9), which is also the mean value approximation over all wall interaction parts (P2, P4, P6) considering the respective standard deviations. Similarly for the torque, when the total energy exceeds the E_{\max} set, the torque magnitude does not exceed 55Nm , the mean value approximation over all wall interaction parts (P2, P4, P6) is 51Nm . The consistency of all mean values being close to the maximum values and of all standard deviation values being low proves the efficiency of the energy layer in restricting the output force and torque in situations that are unsafe for human users ($E_{\text{tot}} \geq E_{\max}$).

Part	Duration while $E_{\text{tot}} \geq E_{\text{max}}$ (s)	Force (N)			Torque (Nm)		
		Max	Mean	Std. Dev.	Max	Mean	Std. Dev.
P2	1.15	57.86	56.71	1.09	54.21	51.86	1.74
P4	2.47	57.35	56.69	0.53	51.42	50.49	0.82
P6	3.53	57.88	57.01	0.68	51.22	49.94	1.00

Table 4.5: The maximum, mean and standard deviation of the force and torque while the total energy (E_{tot}) exceeds the total maximum energy (E_{max}) due to the interaction with the wall (P2, P4 and P6), computed from the filtered data (Figure 4.9).

Herein, the first set of results obtained by following the energy potential definition reported by Fasse (1997) and Stramigioli (2001), and used by Raiola et al. (2018), do not share the offset seen in the rotational potential energy computation. It is unclear how Raiola et al. (2018) did not encounter the same issue and if the tested formula (eq. 4.5) is the proper way to deal with it. Moreover, this requires further investigation which is out of the scope of this project. Nonetheless, the new approach used here, that includes the offset in the rotational potential energy ($V_o(\mathbf{R}_s^{\text{SP}})$), yielded the expected results.

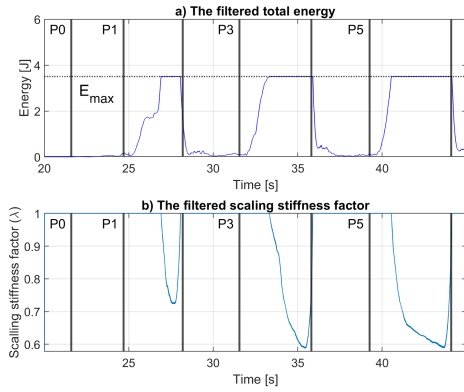


Figure 4.8: The total energy of the system (a) and the stiffness factor λ (b), smoothen with a 5-term moving average filter. The free motion parts are illustrated (P1, P3 and P5) within the figure, while the interaction with the wall (P2, P4 and P6) are not label within the figure.

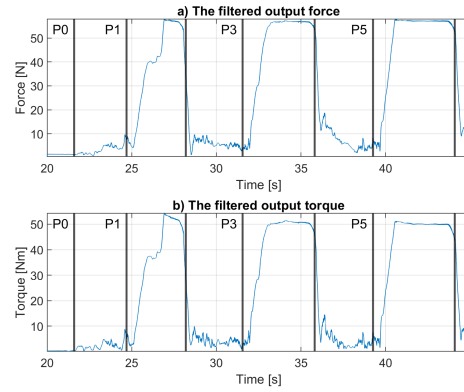


Figure 4.9: The magnitude of the output force (a) and torque (b) of the master device, smoothen with a 5-term moving average filter. The free motion parts are illustrated (P1, P3 and P5) within the figure, while the interaction with the wall (P2, P4 and P6) are not label within the figure.

4.4 Test 3 - A safety test -The power limit

4.4.1 Goal

The goal of this test is to validate the power limit (P_{\max}) set for a safe human handling of the Panda robotic arm as a haptic input device.

4.4.2 Method

To validate the power limit, the power consumed for providing force feedback to the user (P_{c_m}) should either be lower or equal than the P_{\max} or else, a damping scaling term (β) is used to transfer the power difference to the damping matrix (B), which is in turn going to reduce the P_{c_m} (see equations: 3.10, 3.11, 3.12 in Chapter 3).

Similar to the first two tests, for initialization two safety limits are set: 4.5J for the maximum total energy that may be allowed between the master and slave devices; and 140N for the force allowed between the master and user. And unlike the first two tests, for the safety limit herein tested, 5W is set as the maximum power (P_{\max}) allowed between the master and user, in order to reduce the effort required by the user to reach the limit during the experiment.

While viewing on a screen the slave device simulated in Gazebo environment where there is also a virtual wall, the user moves the master end-effector and the slave end-effector follows it towards this wall. When the slave end-effector hits the wall, the slave stops following the master. At this moment the user feels the impact because the master starts pushing back on the user due to the designed force feedback. The user starts pulling the master away from the wall. After the master end-effector reaches again to its initial position, the user repeats the hit all over again twice for reproducibility. The faster the end-effector moves, the higher the power generated from the impact with the virtual wall will be.

4.4.3 Expected results

The interaction that results from the slave end-effector hitting the virtual wall is expected to generate a higher peak power than the set P_{\max} . The damping scaling factor (β in eq. 3.12) is recorded during the experiment and it is expected to increase its value. Moreover, the total scaled power computed with the β factor is expected not to pass the chosen P_{\max} of 5W.

4.4.4 Results and discussion

Figure 4.10 shows how the total power scaled, the scaling damping factor and the position on the X axis for the master and slave end-effectors change with time for all three repetitions that the user performed. The white areas are times when the user does not move the master and the slave is away from the virtual wall, while the grey areas are the wall interaction periods. For each experiment (i.e. each grey area), the power generated starts at zero and it is first slowly decreasing as the user is moving the master device. The negative peak power reached corresponds to -29.3 W, -25.0 W and -22.0 W for each consecutive experiment. At this moment, the slave device hit the virtual wall and stopped following the master (full versus dashed lines in Figure 4.10c). At this moment the master starts pushing back on the user due to the designed force feedback and the power is quickly increasing. The moment it reaches zero is the moment in which the master device starts moving such that the slave would be pulled away from the wall, in the opposite direction of the hitting motion. The power generated by the master device is from now on positive and from the moment it reaches P_{\max} , the damping scaling β starts increasing (Figure 4.10b) to reduce the P_{c_m} such that it will not exceed the 5W power limit. When the slave resumes following the master, the force feedback is also reduced because there is no longer a wall interaction. Now the power is again decreasing as the user is again transferring power to the master. The experiment ends when the master reaches again its initial position.

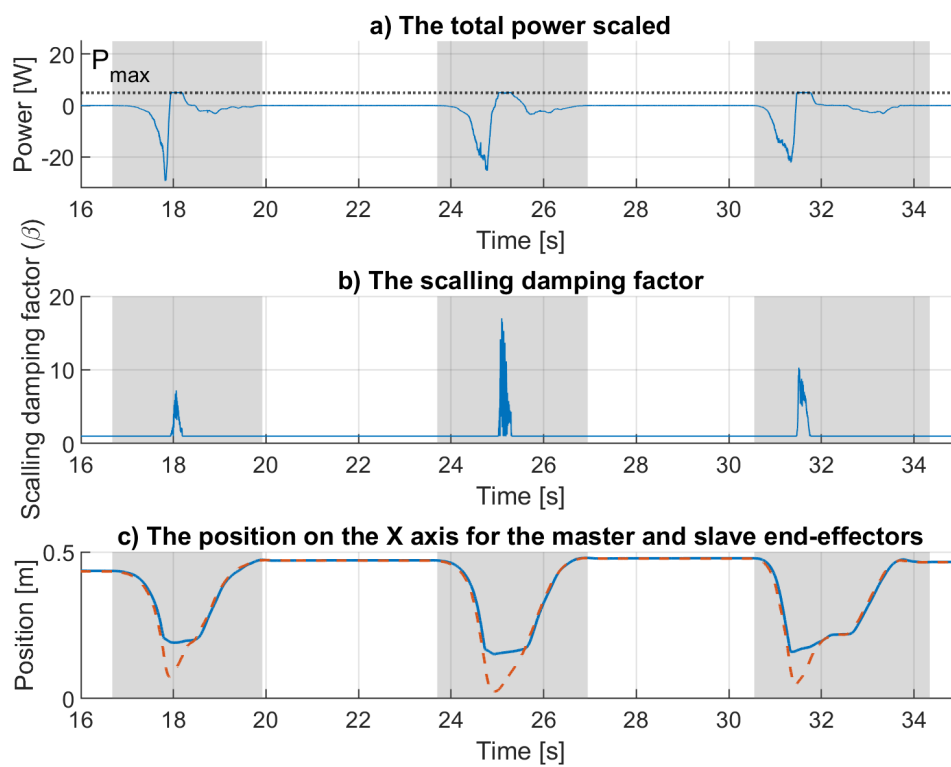


Figure 4.10: The total power scaled (a), the scaling damping factor (b), and the position on the X axis for the master and slave end-effectors (c) change with time. The white areas correspond to the time of no force feedback, while the grey areas correspond to the three experiment periods. The dotted line in a) denotes the 5W power limit set, i.e. P_{max} . The full (blue) and dashed (red) lines in c) correspond to the slave and master end-effectors, respectively.

For this test, the scaled power was monitored by the impedance controller that is used in commanding the joint torques of the master device. This is less accurate than if the actual power of the interaction between the user and the Panda master device would have been independently measured. Nonetheless, the results are as expected, since the power is indeed always less than P_{max} , and the test was successful.

4.5 Test 4 - A safety test - The force limit

4.5.1 Goal

The goal of this test is to validate the force limit (F_{\max}) set for a safe human handling of the Panda robotic arm as a haptic input device.

Within the system, two force limits are implemented: (1) one within the control unit of the Panda robotic arm set conservatively as explained in Chapter 2.1.2 to 80 N for each of the three force axis, and (2) one within the impedance controller located on the slave side. In this section, only the later will be validated because the former is provided and well documented by the Panda's manufacturer.

4.5.2 Method

To validate the force limit, the force computed as part of the wrench output of the impedance controller should be lower in magnitude than the 140 N limit (ISO/TS15066, 2016). However, in order to reduce the effort required by the user to exceed the limit during this experiment, force limit of 30 N is used. This value is also lower than the 60 N reached experimentally when the energy is at its maximum of 3.5 J in the energy limit test. Therefore, it is ensured that the force limit is reached before the energy exceeds its maximum set value in this test.

Similar to the previous tests, for initialization (P0) two safety limits are set: 4.5 J for the maximum total energy that may be allowed between the master and slave devices; and 198 W for the maximum power allowed between the master and user.

While viewing on a screen the slave device simulated in Gazebo, the user moves the master end-effector such that the slave end-effector can be seen approaching the virtual wall. When the slave end-effector is in contact with the wall, the user feels the presence of the wall through the force feedback exerted by the master. At this point, the user increases his force on the master end-effector for a few seconds. The user starts pulling the master away from the wall. After the master end-effector reaches again its initial position, the user repeats the hit all over again twice for reproducibility.

4.5.3 Expected results

During the interaction with the wall, the magnitude force generated by the impedance controller is expected not to exceed the chosen F_{\max} .

4.5.4 Results and discussion

Figure 4.11 shows the change with time for the magnitude force feedback and the position on the X axis for the master and slave end-effectors. The white areas correspond to the time of no force feedback. As the user moves the master end-effector, the force feedback is slowly increasing. When the slave end-effector is in contact with the wall, the force feedback has a steep increase such that the user feels the presence of the wall. However, the magnitude force that the master device outputs to the user does not exceed the F_{\max} of 30 N, as expected. When the user starts pulling the master away from the wall, the force feedback is steeply decreasing until the moment in which the slave starts to follow the master again. Until the master end-effector reaches again its initial position, the force feedback is again slowly increasing and decreasing. The overall shape of the force feedback behaviour with time is, therefore, a sharp peak (wall interaction) flanked by two smaller peaks (free motion). Although, ideally, all dynamic effects, such as inertia Coriolis and gravity compensation, should be compensated for, this was not done and leads to the observation of the aforementioned small peaks.

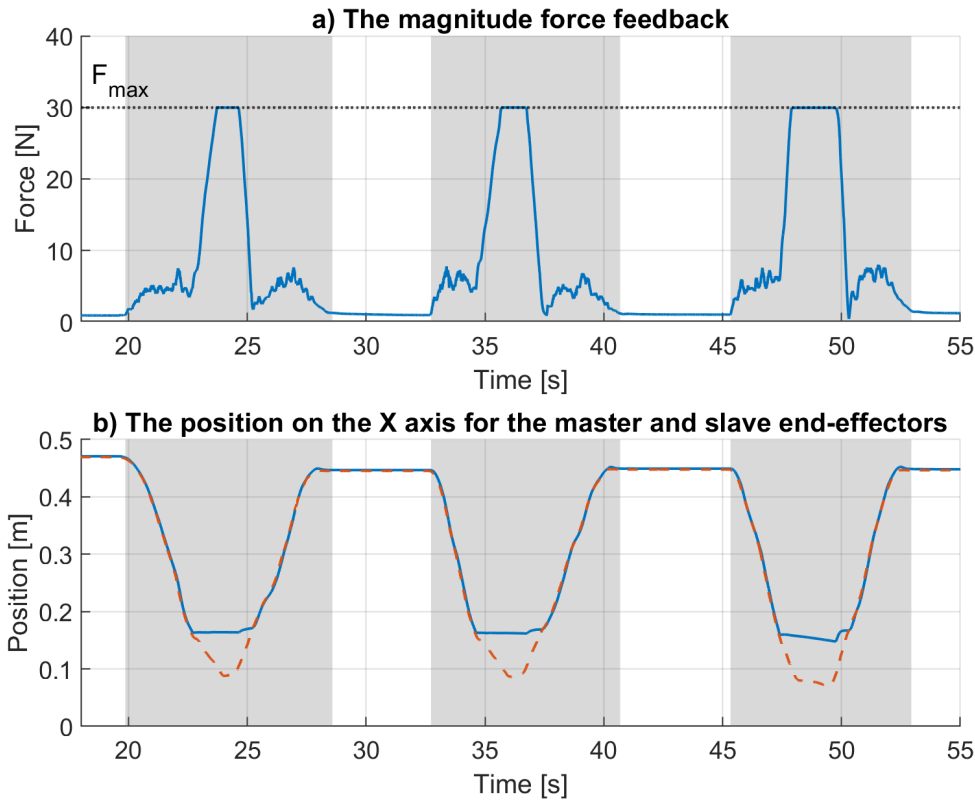


Figure 4.11: The magnitude force feedback (a) that the Panda haptic device exerts on the user and the position on the X axis for the master and slave end-effectors (b) change with time. The white areas correspond to the time of no force feedback, while the grey areas correspond to the three experiment periods. The dotted line in a) denotes the 30N force limit set, i.e. F_{\max} . The full (blue) and dashed (red) lines in b) correspond to the slave and master end-effectors, respectively.

4.6 Evaluation conclusion

The haptic performance test (section 4.2 above) concluded that the implemented system allows the user to move the master device end-effector and receive force feedback from the simulated environment. The slave device end-effector tracks the location and orientation of the master with relatively low mean errors in both position and orientation (see Table 4.3). When interacting with a wall, as expected the mean errors in position and orientation are higher and it is mainly due to the interaction control (i.e. impedance control) parameters.

With the energy limit test (section 4.3 above), the method was not validated using the definitions of the potential energy stored in the spatial spring (eq. 3.4) as found in literature (Tadele, 2014). Therefore, a more practical method to obtain the desired output was implemented and tested, however, further research is required to validate if this is the proper way of dealing with the issue. In terms of force, although the limit set was 140N, the maximum reached was 60N because that corresponds already to the 3.5J set energy limit.

With the force limit test (section 4.5 above), the method was validated using a set limit of 30N instead of the force limit of 140N (ISO/TS15066, 2016). The lower limit was chosen such that the user is able to perform the test more comfortably, by not having to consume much energy to test a higher force limit.

The power limit test (section 4.5 above) concluded that the power is indeed limited to 5W, as set. However an external system should be used in the future to accurately measure the interaction power.

In conclusion, three of the four tests validated the methods used and an alternative method was validated for the unsuccessful validation of the fourth (i.e. the energy limit test).

5 Conclusion and recommendations

5.1 Conclusions

This project set out to improve the telemanipulation of a KUKA LWR 4+ robotic arm by replacing the omega.7 haptic device currently used to control it with another robotic arm (i.e. the Emika Franka Panda robotic arm). Towards this end, two main research questions were addressed:

1. *"How can the Panda robotic arm be safely used in interaction with humans?"*
2. *"How can the Panda robotic arm be effectively used as a haptic interface device?"*

For the first research question, a safety precaution for the human-robot interface, a geo-fencing constraint, energy, power and force limitations were considered in the Analysis chapter (see section 2.1) as essential parts of the safe telemanipulation system. From these, the first two limits were not implemented due to time constraints. Herein, the limitations considered are energy, power and force. These were implemented and evaluated on a system controlling the computer simulated model of a KUKA LWR 4+ robotic arm. The set limit values used for validation are presented in Table 4.2 (see section 4.1).

The energy that Panda robotic arm may transfer to the human operator is limited to a value that represents a safety threshold, above which the user might be harmed. The force that Panda robotic arm may exert on the human operator is limited to a value that corresponds to the highest force that the user may withstand without pain at hand level, as defined in the industrial robotics standard (ISO). The power that Panda robotic arm may instantaneously transfer to the human operator during an impact is limited to a value that represents a safety threshold, above which irreversible damage might occur to the user.

The tests performed showed that the implemented algorithm can effectively enforce the specified limits only for the power and the force constrains. The energy constrain was not validated. The application of the energy limit using the method reported by Fasse (1997) gave unexpected results; that method did not allow for a zero starting total energy. The definitions of the potential energy stored in the spatial spring resulted in the unexpected result of -75J for the starting energy, given the chosen controller parameters. Therefore, the output force and torque were not adequately restricted, and the user safety could not be guaranteed as such. It is unclear how Raiola et al. (2018) did not encounter the same issue in their presented experiments.

Herein, another approach to obtain the desired output was implemented and tested where the -75J was treated as an offset. This approach mitigated the offset, which was also done implicitly by Raiola et al. (2018), and allowed the expected zero starting total energy and the effective application of the energy bounds in the system. However, this approach was not verified for its mathematical and physically correctness.

For the second research question, the optimal workspace and continuous output force of the Panda robotic arm were discussed in the Analysis chapter (see section 2.2). The Panda robotic arm has the potential to be used as a haptic input device, as long as its position carefully aligns the robotic with the human arm workspace. Herein, the force is limited to one third of the maximum force of the human arm within the reachable workspace. Moreover, a haptic test was performed for evaluation, to validate that (1) the end-effector of the slave follows that of the master device and (2) a proper force feedback is established between them. The results showed that the implemented system allows indeed the user to move the master device end-effector and receive force feedback from the simulated environment.

In conclusion, the goals of this project were successfully met. A control methodology was developed and implemented for the i-Botics telemanipulation system such that the Emika Franka Panda robotic arm could safely be used by humans as input haptic device for the KUKA LWR 4+.

5.2 Recommendations

Based on the results of this work several suggestions can be made for continuation.

Firstly, it was noted that a safe human-robot interface is an essential part of such safe telemanipulation system which was not covered in this research. This should be designed and implemented to eventually complete the safe telemanipulation system.

Secondly, the geo-fencing feature through the virtual walls will be beneficial in guaranteeing the safety of the operator as well as preventing the robot collisions that will damage its hardware. However the implemented "VirtualWallCuboid" as provided by the software of the Emika Franka Panda robotic arm could not be validated due to the delay of the corresponding software update release date. Therefore, the desired behaviour of the Panda robotic arm in combination with the virtual walls should be validated in the future, as soon as the new software is released.

Thirdly, the tests were currently performed based on the internal sensors of the Panda robotic arm and did give some level of validation. However, more reliable tests could be performed using independent external sensors such as force and motion sensors. For example, the power could be measured using an external force sensor attached to the end-effector of the Panda and an optical system to track the position of the end-effector.

Fourthly, since the energy limit test could not validate the constrain as originally formulated and an alternative approach resulted in the expected outcome, for future development of the project, the mathematical and physical correctness of potential energy definitions of the alternative presented herein should be investigated.

Fifthly, regarding the robotic arm, a recommendation is made for the installation setup based on the analysis of Zacharias et al. (2010) that considered two scenarios for aligning the robotic with the human arm workspace. For this project, scenario 2 (see Figure 2.4b, Chapter 2.2.3) is recommended. In that case, the right arm of the human interacts with the right arm of the robotic system. By repositioning the human shoulder with respect to the robotic system, the area of the region where the maximum coverage occurs is found to be greater in scenario 2 compared with scenario 1, making the former a viable option for the future development of this project.

Finally, the future follow-up projects should move forward to using the real hardware and as a consequence address the possible factors affecting the system stability such as network communication delays. Therefore, implementation of passivity layers as described by Franken et al. (2011) is recommended for the future development of this novel use of a robotic arm as an input haptic device to control the KUKA LWR 4+ in remote and hostile environments.

A Screw theory applied to human arm kinematics

The goal of applying screw theory to human arm kinematics is to relate the joint torques to the Cartesian forces. Towards this end, the geometrical Jacobian is computed (section A.1) and applied in the algorithm described in section A.2.

A.1 Building the geometrical Jacobian

The following steps are performed on the arm model (Figure 2.5) as explained in detailed by Stramigioli and Bruyninckx (2001):

1. In joint configuration zero, the difference between coordinate frames are:

$$p_1^0 = p_2^1 = p_3^2 = \begin{bmatrix} 0 \\ 0 \\ 0 \end{bmatrix}, p_4^3 = \begin{bmatrix} -L1 \\ 0 \\ 0 \end{bmatrix}, p_5^4 = \begin{bmatrix} -L2 \\ 0 \\ 0 \end{bmatrix}, p_6^5 = p_7^6 = \begin{bmatrix} 0 \\ 0 \\ 0 \end{bmatrix} \quad (\text{A.1})$$

where the two links of the human arm model are defined as $L1$ and $L2$ equal with 0.2m and 0.25m, respectively.

2. The human arm model consists of only rotational joint, of which unit rotations are assigned:

$$\omega_1^{0,0} = \begin{bmatrix} 0 \\ 0 \\ 1 \end{bmatrix}, \omega_2^{1,1} = \begin{bmatrix} 0 \\ -1 \\ 0 \end{bmatrix}, \omega_3^{2,2} = \begin{bmatrix} -1 \\ 0 \\ 0 \end{bmatrix}, \omega_4^{3,3} = \begin{bmatrix} 0 \\ -1 \\ 0 \end{bmatrix}, \omega_5^{4,4} = \begin{bmatrix} -1 \\ 0 \\ 0 \end{bmatrix}, \omega_6^{5,5} = \begin{bmatrix} 0 \\ -1 \\ 0 \end{bmatrix}, \omega_7^{6,6} = \begin{bmatrix} 0 \\ 0 \\ -1 \end{bmatrix} \quad (\text{A.2})$$

3. The direction of rotation for each joint is purely along an axis of the attached coordinate frame. All the coordinate frames are in the same orientation as frame 0 (inertial frame) and are not illustrated in Figure 2.5. Therefore H-matrices (also known as homogeneous transformation matrix) that describes the relative position of a coordinate frame to the linked coordinate frame are summarize in table A.1.

For example, R_{z-pos} is the rotation matrix for a rotation around Z axis in positive direction (using right hand rule), if it is negative, the *sin* terms get their signs inverted.

The H-matrix that expresses the last frame in inertial frame is obtain by multiplying the homogeneous matrices:

$$H_n^0 = H_1^0 H_2^1 \dots H_n^{n-1} \quad (\text{A.3})$$

4. A general velocity can be written as a twist in vector form:

$T_a^{c,b} = [\omega_x, \omega_y, \omega_z, v_x, v_y, v_z]^T$, which denotes the twist of frame a with respect to frame b expressed in frame c . Where v is the cross product of p and ω : $v = p \times \omega$. For each of the joints, the unit twists in inertial frame (frame 0) with respect to previous frame, expressed in previous frame is computed as:

$$\hat{T}_n^{n-1,n-1} = \begin{bmatrix} \omega_n^{n-1,n-1} \\ p_n^{n-1} \times \omega_n^{n-1,n-1} \end{bmatrix} \quad (\text{A.4})$$

5. Finally, the geometric Jacobian that maps the joint velocities $\dot{\mathbf{q}} = [\dot{q}_1, \dot{q}_2, \dots, \dot{q}_n]^T$ to end effector velocity with respect to inertial frame expressed in inertial frame is: (see Stramigioli and Bruyninckx (2001) if interested in the proof)

$$J(\mathbf{q}) = [T_1^{0,0}(q_1) \quad T_2^{0,1}(q_2) \quad \dots \quad T_n^{0,n-1}(q_n)] \quad (\text{A.5})$$

with

$$T_n^{0,n-1} = \text{Ad}_{H_{n-1}^0(q_n)} \hat{T}_n^{n-1,n-1} \quad (\text{A.6})$$

and

$$\text{Ad}_{H_{n-1}^0} = \begin{bmatrix} R_{n-1}^0 & \mathbf{0} \\ p_{n-1}^0 \times R_{n-1}^0 & R_{n-1}^0 \end{bmatrix} \quad (\text{A.7})$$

such that

$$T_n^{0,0} = J(\mathbf{q})\dot{\mathbf{q}} \quad (\text{A.8})$$

$$H_1^0 = \begin{pmatrix} R_{z-pos} & \mathbf{0}_3 \\ \mathbf{0}_3 & 1 \end{pmatrix} = \begin{pmatrix} c & -s & 0 & 0 \\ s & c & 0 & 0 \\ 0 & 0 & 1 & 0 \\ 0 & 0 & 0 & 1 \end{pmatrix} \quad H_2^1 = \begin{pmatrix} R_{y-neg} & \mathbf{0}_3 \\ \mathbf{0}_3 & 1 \end{pmatrix} = \begin{pmatrix} c & 0 & -s & 0 \\ 0 & 1 & 0 & 0 \\ s & 0 & c & 0 \\ 0 & 0 & 0 & 1 \end{pmatrix}$$

$$H_3^2 = \begin{pmatrix} R_{x-neg} & \mathbf{0}_3 \\ \mathbf{0}_3 & 1 \end{pmatrix} = \begin{pmatrix} c & -s & 0 & 0 \\ s & c & 0 & 0 \\ 0 & 0 & 1 & 0 \\ 0 & 0 & 0 & 1 \end{pmatrix} \quad H_4^3 = \begin{pmatrix} R_{y-neg} & p_4^3 \\ \mathbf{0}_3 & 1 \end{pmatrix} = \begin{pmatrix} c & -s & 0 & -L_1 \\ s & c & 0 & 0 \\ 0 & 0 & 1 & 0 \\ 0 & 0 & 0 & 1 \end{pmatrix}$$

$$H_5^4 = \begin{pmatrix} R_{x-neg} & p_5^4 \\ \mathbf{0}_3 & 1 \end{pmatrix} = \begin{pmatrix} c & -s & 0 & -L_2 \\ s & c & 0 & 0 \\ 0 & 0 & 1 & 0 \\ 0 & 0 & 0 & 1 \end{pmatrix} \quad H_6^5 = \begin{pmatrix} R_{y-neg} & \mathbf{0}_3 \\ \mathbf{0}_3 & 1 \end{pmatrix} = \begin{pmatrix} c & 0 & -s & 0 \\ 0 & 1 & 0 & 0 \\ s & 0 & c & 0 \\ 0 & 0 & 0 & 1 \end{pmatrix}$$

$$H_7^6 = \begin{pmatrix} R_{z-neg} & \mathbf{0}_3 \\ \mathbf{0}_3 & 1 \end{pmatrix} = \begin{pmatrix} c & 0 & -s & 0 \\ 0 & 1 & 0 & 0 \\ s & 0 & c & 0 \\ 0 & 0 & 0 & 1 \end{pmatrix}$$

Table A.1: The H matrices between the joint frames. The c and s represent the cos and sin, respectively and the angle notation is omitted for brevity.

A.2 Pseudo-code for obtaining the maximum force

In this section the algorithm used to calculate the maximum force the human arm can achieve in the workspace based on a 7 degree of freedom model (Toussaint et al., 2005) is presented.

The algorithm core is based on the equation 2.7, such that the joint torques are calculated from the wrench and the Jacobian. It is stored the maximum force that can be achieved without exceeding the human arm maximum torques (table 2.6) and known force threshold (Das and Wang, 2004). This way, the maximum force is related to the location in the reachable workspace of the human arm.

The reachable workspace is obtain from all combinations of the 7 joints that define the human arm model. In detail, the range for each joint (table 2.6) is discretized into 5 values, resulting in a total possible joint configurations of 5^7 combinations. From the total joint configuration possible, multiple configurations result in the same location of the hand within the reachable

workspace. By defining the reachable Cartesian workspace as multiple 5 cm^3 boxes, one maximum force can be calculated for each box. Each box is defined by 3 parameters relating to the X, Y and Z position in the Cartesian space. The considered Cartesian space is ranging from -0.5m to 0.5m with increments of 0.05m for each X, Y and Z axis. The length of the human arm model is composed of 2 links, measuring 0.2 and 0.25 . For each joint configuration of the human arm, the hand location is calculated using homogeneous matrix (eq. A.3) and is stored in a box of the reachable workspace. Using the joint configuration for each box in the reachable workspace, the maximum force is computed using Algorithm 1.

Algorithm 1: The algorithm used for computing the maximum forces a human arm outputs within the reachable workspace discretized in boxes of 5 cm^3 .

input : q - 7 joint positions for the 7DOF human arm
Box - a 5 cm^3 volume within the reachable workspace of the human arm
 $J(q)^\top$ - transpose of the Jacobian in a q joint configuration
 τ_{max} - maximum torques of the 7DOF human arm
output: *MaxForce* - array containing all the maximum forces for each *Box*.

```

1 foreach Box do
2   foreach  $q \in \text{Box}$  do
3     ForceXaxis  $\leftarrow 0$ ;
4     while  $\tau < \tau_{max}$  or  $\text{ForceXaxis} \leq 400$  do
5       Wrench  $\leftarrow \text{ForceXaxis}$ ; /* Only 1 component of Wrench is
6         assigned a value, rest are 0. */
7        $\text{Wrench}^0 \leftarrow \text{Ad}_{H_0}^\top \text{Wrench}$ ; /* The wrench expressed in hand
8         frame is expressed to inertial frame. */
9        $\tau \leftarrow J(q)^\top \text{Wrench}^0$ ; /* equation 2.8 */
10      ForceXaxis++;
11    end
12    Forces( $q$ )  $\leftarrow \text{ForceXaxis}$ ;
13 end

```

The Algorithm 1 was performed three times for computing the force on all three axis.

B Results for test 2 - A safety test - The energy limit

With the safety test 2 described in Ch4, the energy limit, the total energy of the system (eq. 3.1 in Chapter 3) defined as the sum of the kinetic energy of the master device, and the potential energy due to the spatial spring should either be lower or equal with E_{\max} or else, a factor term (λ) is used to reduce the computed wrench (W_p) applied to the user by the Panda robotic arm. The results for both energy and force before filtering out the noise is shown in Figures B.2 and B.1. Note that, all signals measured during the wall interaction P2, P4 and P6 have a noisy peak. The clean signal results obtained with a 5-term moving average filter are shown in the main text (see Figure 4.8 and Figure 4.9).

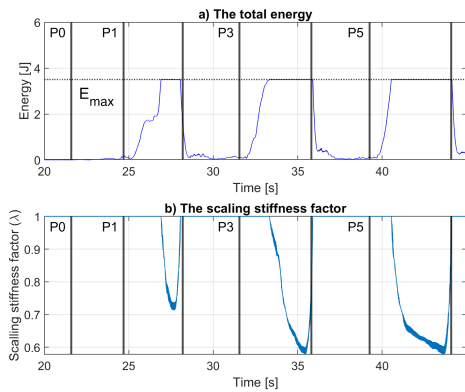


Figure B.1: The total energy of the system (a) and the stiffness factor λ (b). The free motion parts are illustrated (P1, P3 and P5) within the figure, while the interaction with the wall (P2, P4 and P6) are not label within the figure.

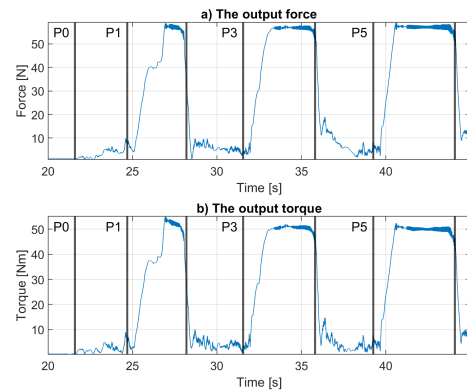


Figure B.2: The magnitude of the output force (a) and torque (b) of the master device. The free motion parts are illustrated (P1, P3 and P5) within the figure, while the interaction with the wall (P2, P4 and P6) are not label within the figure.

This noisy behavior makes the system momentarily unstable and the reason for it should be considered for future troubleshooting. So far, one hypothesis could be that the scaling stiffness factor (λ) is faultily computed within the impedance controller general component (see section 3.3.1).

Bibliography

- ANSI/RIA-R15.06 (2012), Industrial Robots And Robot Systems - Safety Requirements, AN-SI/RIA R15.06-2012, Robotic Industries Association.
- Butler, J. T. and A. Agah (2001), Psychological effects of behavior patterns of a mobile personal robot, **vol. 10**, no.2, pp. 185–202.
- Campa, R. and H. De La Torre (2009), Pose control of robot manipulators using different orientation representations: A comparative review, in *2009 American Control Conference*, IEEE, pp. 2855–2860.
- Carignan, C., M. Liszka and S. Roderick (2005), Design of an arm exoskeleton with scapula motion for shoulder rehabilitation, in *ICAR'05. Proceedings., 12th International Conference on Advanced Robotics, 2005*.
- Das, B. and Y. Wang (2004), Isometric pull-push strengths in workspace: 1. Strength profiles, **vol. 10**, no.1, pp. 43–58.
- Dined (2004), Anthropometric database, Faculty of Industrial Design Engineering, Delft University of Technology.
<https://www.dined.nl/>
- Ellery, D. (2017), Writing reusable code for robotics.
- EMIKA, F. (2017), TECHNICAL DATA FRANKA EMIKA - industry, website accessed on: 01-05-2017.
https://s3-eu-central-1.amazonaws.com/franka-de-uploads-staging/uploads/2017/05/2017-05-12_datasheet-industry.pdf
- EMIKA, F. (2018), TECHNICAL DATA Panda, website accessed on: 01-09-2018.
<https://s3-eu-central-1.amazonaws.com/franka-de-uploads-staging/uploads/2018/05/2018-05-datasheet-panda.pdf>
- Erden, M. S. and A. Billard (2014), End-point impedance measurements at human hand during interactive manual welding with robot, in *2014 IEEE international conference on robotics and automation (ICRA)*, IEEE, pp. 126–133.
- Fasse, E. D. (1997), On the spatial compliance of robotic manipulators, **vol. 119**, no.4, pp. 839–844.
- Flacco, F., T. Kröger, A. D. Luca and O. Khatib (2012), A depth space approach to human-robot collision avoidance, in *2012 IEEE International Conference on Robotics and Automation*, pp. 338–345, ISSN 1050-4729, doi:10.1109/ICRA.2012.6225245.
- ForceDimension (2019), Force Dimension Omega.7, website accessed on: 08-03-2019.
<http://www.forcedimension.com/products/omega-7/overview>
- Franken, M., S. Stramigioli, S. Misra, C. Secchi and A. Macchelli (2011), Bilateral telemanipulation with time delays: A two-layer approach combining passivity and transparency, **vol. 27**, no.4, pp. 741–756.
- Haddadin, S., A. Albu-Schaffer, A. D. Luca and G. Hirzinger (2008), Collision detection and reaction: A contribution to safe physical Human-Robot Interaction, in *2008 IEEE/RSJ International Conference on Intelligent Robots and Systems*, pp. 3356–3363, ISSN 2153-0858, doi:10.1109/IROS.2008.4650764.
- Haddadin, S. and E. Croft (2016), *Physical Human–Robot Interaction*, Springer International Publishing, pp. 1835–1874, ISBN 978-3-319-32552-1, doi:10.1007/978-3-319-32552-1_69.

- Hashtrudi-Zaad, K. and S. E. Salcudean (2001), Analysis of control architectures for teleoperation systems with impedance/admittance master and slave manipulators, **vol. 20**, no.6, pp. 419–445.
- Howard, I. S., J. N. Ingram, K. P. Körding and D. M. Wolpert (2009), Statistics of natural movements are reflected in motor errors, **vol. 102**, no.3, pp. 1902–1910.
- Hulin, T., M. Sagardia, J. Artigas, S. Schaetzle, P. Kremer and C. Preusche (2008), Human-scale bimanual haptic interface, *Enactive08*, pp. 28–33.
- ISO10218-1 (2011), Robots and Robotic Devices - Safety Requirements for Industrial Robots - Part 1: Robots, ISO 10218-1:2011, International Organization for Standardization, Geneva.
- ISO10218-2 (2011), Robots and Robotic Devices - Safety Requirements for Industrial Robots - Part 2: Robot systems and integration, ISO 10218-2:2011, International Organization for Standardization, Geneva.
- ISO13849, E. (2008), 13849-1, *Safety of machinery—Safety-related parts of control systems—Part*, **vol. 1**, pp. 13849–1.
- ISO/TS15066 (2016), Robots and robotic devices – Collaborative robots, ISO/TS 15066:2016, International Organization for Standardization, Geneva.
- KUKA Roboter GmbH (2012), Lightweight Robot 4+ specification.
- Lasota, P. A., T. Fong, J. A. Shah et al. (2017), A survey of methods for safe human-robot interaction, **vol. 5**, no.4, pp. 261–349.
- Lawrence, D. A. (1993), Stability and transparency in bilateral teleoperation, **vol. 9**, no.5, pp. 624–637.
- Letier, P., M. Avraam, S. Veillerette, M. Horodinca, M. De Bartolomei, A. Schiele and A. Preumont (2008), SAM: A 7-DOF portable arm exoskeleton with local joint control, in *Intelligent Robots and Systems, 2008. IROS 2008. IEEE/RSJ International Conference on*, IEEE, pp. 3501–3506.
- Meguenani, A. (2017), *Safe Control of Robotic Manipulators in Dynamic Contexts*, Theses, Université Pierre & Marie Curie - Paris 6 ; Institut des Systèmes Intelligents et de Robotique. <https://hal.archives-ouvertes.fr/tel-01620663>
- Mumm, J. and B. Mutlu (2011), Human-robot proxemics: Physical and psychological distancing in human-robot interaction, in *2011 6th ACM/IEEE International Conference on Human-Robot Interaction (HRI)*, pp. 331–338, ISSN 2167-2148, doi:10.1145/1957656.1957786.
- Newman, J. A. and N. Shewchenko (2000), A proposed new biomechanical head injury assessment function-the maximum power index, Technical report, SAE Technical Paper.
- Nijhof, S. (2018), Teleoperation using passive control and LUNA network channels.
- O'Malley, M. and M. Goldfarb (2002), The effect of force saturation on the haptic perception of detail, **vol. 7**, no.3, pp. 280–288.
- Plooij, M., G. Mathijssen, P. Cherule, D. Lefeber and B. Vanderborght (2015), Lock Your Robot: A Review of Locking Devices in Robotics, **vol. 22**, no.1, pp. 106–117, ISSN 1070-9932, doi:10.1109/MRA.2014.2381368.
- Rader, S., L. Kaul, P. Weiner and T. Asfour (2017), Highly integrated sensor-actuator-controller units for modular robot design, in *2017 IEEE International Conference on Advanced Intelligent Mechatronics (AIM)*, IEEE, pp. 1160–1166.
- Radi, M. and G. Reinhart (2009), Industrial Haptic Robot Guidance System for assembly processes, in *2009 IEEE International Workshop on Haptic Audio visual Environments and Games*, pp. 69–74, doi:10.1109/HAVE.2009.5356135.

- Raiola, G., C. A. Cardenas, T. S. Tadele, T. de Vries and S. Stramigioli (2018), Development of a Safety-and Energy-Aware Impedance Controller for Collaborative Robots, **vol. 3**, no.2, pp. 1237–1244.
- Rocha, C., C. Tonetto and A. Dias (2011), A comparison between the Denavit–Hartenberg and the screw-based methods used in kinematic modeling of robot manipulators, **vol. 27**, no.4, pp. 723–728.
- Ruedi, T., R. Buckley and C. Moran (2007), *AO principles of fracture management*, Thieme.
- Srinivasan, M. A. (1995), What is haptics?, *Laboratory for Human and Machine Haptics: The Touch Lab, Massachusetts Institute of Technology*, pp. 1–11.
- Stramigioli, S. (1998), *From differentiable manifold to interactive robot control*, Ph.D. thesis, TU Delft, Delft University of Technology.
- Stramigioli, S. (2001), *Modeling and IPC control of interactive mechanical systems—A coordinate-free approach*.
- Stramigioli, S. and H. Bruyninckx (2001), Geometry and screw theory for robotics, *Tutorial during ICRA*, **vol. 2001**, p. 75.
- Sun, X., K. Andersson and U. Sellgren (2017), Design optimization of haptic device-A systematic literature review.
- Tadele, T. S. (2014), *Human-friendly robotic manipulators: safety and performance issues in controller design*, Phd thesis, University of Twente.
- Teeffelen, v. K. (2018), Intuitive Impedance Modulation in Haptic Control using Electromyography.
- Tondu, B., S. Ippolito, J. Guiochet and A. Daidie (2005), A seven-degrees-of-freedom robot-arm driven by pneumatic artificial muscles for humanoid robots, **vol. 24**, no.4, pp. 257–274.
- Wood, J. L. (1971), Dynamic response of human cranial bone, **vol. 4**, no.1, pp. 3–12.
- Yoganandan, N., F. Pintar, D. Maiman, J. Cusick, A. Sances Jr and P. Walsh (1996), Human head-neck biomechanics under axial tension, **vol. 18**, no.4, pp. 289–294.
- Zacharias, F., C. Borst and G. Hirzinger (2007), Capturing robot workspace structure: representing robot capabilities, in *Intelligent Robots and Systems, 2007. IROS 2007. IEEE/RSJ International Conference on*, Ieee, pp. 3229–3236.
- Zacharias, F., I. S. Howard, T. Hulin and G. Hirzinger (2010), Workspace comparisons of setup configurations for human-robot interaction, in *Intelligent Robots and Systems (IROS), 2010 IEEE/RSJ International Conference on*, IEEE, pp. 3117–3122.